Received 11 June 2021; revised 12 July 2021; accepted 15 July 2021. Date of publication 19 July 2021; date of current version 30 July 2021.

Digital Object Identifier 10.1109/OJCOMS.2021.3098105

Dimming-Based Modulation Schemes for Visible Light Communication: Spectral Analysis and ISI Mitigation

RISHU RAJ [1], SONU JAISWAL [2], AND ABHISHEK DIXIT [1]

[1] Department of Electrical Engineering, Indian Institute of Technology Delhi, New Delhi 110016, India

[2] Research and Development Department (Digital), Espressif Systems, Pune 411045, India

CORRESPONDING AUTHOR: R. RAJ (e-mail: rishu.raj@ee.iitd.ac.in)

This work was supported by the Department of Telecommunications, Ministry of Communications, India, through the Indigenous 5G Test Bed Project.

ABSTRACT Visible light communication (VLC) is being envisioned as an enabling technology to provide the much-needed spectral relief for the ever-increasing demand for Internet connectivity and data consumption. Since VLC uses illumination sources for lighting as well as communication, it is required to provide dimming control for proper lighting and enhanced error performance for reliable data communication. In this paper, we address both these issues holistically. We formulate and study the power spectral densities of dimming-based modulation schemes, namely variable on-off keying (VOOK) and variable pulse position modulation (VPPM), and hence, derive their bandwidth requirements and spectral efficiencies. Moreover, the capacity of VLC systems is severely limited by the inter-symbol interference (ISI) occurring as a result of the multipath propagation of light signals in VLC. We propose to ameliorate the error performance of VLC systems by using channel equalization for ISI mitigation, thereby enhancing the system capacity. We develop the analytical model of a dimmable VLC system employing channel equalization and use this model to study the effect of dimming and data rate on the error performance of VOOK and VPPM schemes. We present simulation and analytical results to show that the performance of dimming-based modulation schemes is significantly improved using channel equalization.

INDEX TERMS Dimming, ISI mitigation, channel equalization, visible light communication.

I. INTRODUCTION

THE International Telecommunication Union has predicted that, by 2030, the global mobile traffic volume is expected to increase by 670 times of that in 2010 which would demand a data traffic volume of over 5 ZB/month, where 1 ZB $= 10^{21}$ bytes [1]–[3]. This dramatic increase in the number of data-hungry devices connected to the Internet has created an urgent need to explore the untapped and unlicensed regions of the electromagnetic spectrum. To this end, the upcoming disruptive optical wireless communication technology called visible light communication (VLC) promises tremendous expansion of spectrum resources by opening up the hitherto untapped visible range of the electromagnetic spectrum for mobile communications [4], [5].

Besides the benefits of license-free spectrum reuse and higher bandwidth, VLC offers several other advantages like radiation safety, less electromagnetic interference, higher energy efficiency, and more security from eavesdroppers as compared to conventional wireless communication technologies [6]. Most of these advantages are attributed to the high efficiency, compact size, long life, and low cost of the white light-emitting diodes (LEDs) used therein [7]. However, in such dual functionality applications, where LEDs are employed both as a communication source and an illumination device, it is desirable to have efficient and reliable data communication and dimming control for brightness regulation. Dimming control provides variable levels of lighting and ensures that data communication is not hindered when a user arbitrarily changes the brightness level of the LEDs. Proper dimming support facilitates power savings, improves energy efficiency, and has ecological benefits. As such, dimming control has been identified

as an essential consideration for VLC by the IEEE 802.15.7 task group [8], [9].

To understand and implement dimming support, it is essential to appreciate the physiology behind how the human eye perceives brightness. The human eye responds to different light levels by dilating or constricting its pupil, in order to allow more or less light to enter the eye, respectively. However, this eye response is non-linear with respect to dimming which results in a difference between the perceived brightness level (δ_p) and the actual brightness level (δ_a), both measured as a fraction of their respective maximum values. These are related as $\delta_p = \sqrt{\delta_a}$ [10]. For example, a lamp that is perceived by the human eye as being dimmed to 22%, is actually dimmed to 5%. Hence, it is required to provide dimming support over a large range and, at the same time, maintain reliable data communication. To this end, the dual objective of dimming control and data transmission is achieved by incorporating dimming techniques into the modulation schemes that are popularly used in other types of optical wireless communication techniques like free space infrared (IR) communication.

While the problem of dimming control exists only in VLC, the detrimental effects of inter-symbol interference (ISI) plague all types of wireless communication systems which are inherently multipath in nature. ISI, which is caused due to the multipath propagation of signals, puts an upper limit on the achievable data rate in a communication system. However, the adverse effects of ISI are more severe in VLC as compared to other wireless communication technologies. This is due to the broadcasting nature of spatially distributed LED transmitters, and the relatively closed and confined indoor environment in which VLC is employed. These two factors result in a very large number of successive reflections, thereby leading to significant variations in the effective path lengths of different signal components carrying the same information. Hence, ISI is a serious concern for high data rate VLC systems.

The most commonly used ISI mitigation technique is channel equalization in which the dispersive effect of the multipath channel is reduced or completely removed by using equalizers at the receiver. The two most popular linear equalizers are the zero-forcing equalizer (ZFE) and the minimum mean square error equalizer (MMSE). ZFE is the simplest equalizer, but it entails noise enhancement at the receiver. The MMSE is complex but does not enhance noise. Interestingly, if the value of signal to noise ratio (SNR) is high (which is the usual case for VLC) then MMSE works as ZFE [11]. However, the linear equalizers cannot mitigate the ISI when the channel noise and distortions become too severe [11]. In that case, non-linear equalization techniques are required. Nevertheless, since VLC is primarily an indoor communication technology, it generally operates at high SNR and low distortion (due to negligible effects of fading). Therefore, ZFE suffices for ISI mitigation in VLC.

A. RELATED WORK

Brightness control and data transmission have been mostly addressed as separate research areas in the literature available on VLC. In this section, we present a review of the literature related to our work on dimming control and ISI mitigation in VLC.

1) DIMMING CONTROL

In the 1990s, several variations of the pulse position modulation (PPM) scheme were proposed to enhance bandwidth (BW) efficiency of IR systems [12], [13]. These include multiple pulse position modulation (MPPM) in [14]–[16] and overlapping pulse position modulation (OPPM) in [17]–[19]. However, they do not provide any inherent dimming support. One of the first attempts to develop a dimming-based modulation scheme is presented by authors in [9], where the 2-PPM modulation is modified to variable pulse position modulation (VPPM) scheme to provide dimming control by varying the pulse widths. They also suggest the use of another scheme called variable on-off keying (VOOK) which is a modification of the on-off keying (OOK) scheme popularly used in optical communication.

Later, authors in [20], [21] and [22] adapted the MPPM and OPPM schemes, respectively, to incorporate the provision for dimming control by changing the number of pulses being transmitted in each symbol. The spectral efficiencies and power requirements of VOOK, VPPM and MPPM are studied in [20], where the authors show that the spectral efficiency of MPPM is higher than that of VOOK and VPPM.

Recently, authors in [23] and [24] have further explored dimming using MPPM. While [23] attempts to achieve enhanced spectral efficiency by combining MPPM with reverse polarity optical orthogonal frequency division multiplexing (RPO-OFDM), [24] studies the encoding and decoding algorithms required for MPPM. However, as also acknowledged by these works [20]–[24], the practical implementation of MPPM is very difficult because its cardinality (number of possible symbols that can be transmitted) depends on the dimming level. So, each time the user adjusts the dimming level, the cardinality and hence, the symbol mapping changes. Consequently, in both MPPM and OPPM, the receiver needs to estimate the dimming level accurately and then re-calibrate the symbol mapping for proper demodulation and correct detection of the received signal. This greatly aggravates the complexity of the receiver architecture and increases latency, especially if the dimming control is required to be done in real-time.

On the other hand, the cardinality and mapping of VOOK and VPPM signals are independent of the dimming value. Hence, they are much simpler to demodulate because each symbol always contains only one pulse, irrespective of the dimming level. However, some amount of performance loss is incurred by choosing a lower complexity scheme. Specifically, using VOOK or VPPM instead of MPPM incurs a power penalty of approximately 2.5 dB, 1.5 dB, 1.5 dB

and 2.5 dB at dimming levels of 0.2, 0.4, 0.6, and 0.8, respectively [20]. Moreover, if VOOK is used instead of MPPM, then at $\gamma = 0.2$, 0.4, 0.6 and 0.8, the spectral efficiency degrades by approximately 20%, 10%, 10% and 20%, respectively [20]. Similarly, at the same dimming levels, using VPPM instead of MPPM deteriorates the spectral efficiency by approximately 40%, 45%, 45% and 40%, respectively [20].

The problem of low spectral efficiencies of these binary schemes can be ameliorated by using them in conjunction with popular multiplexing techniques like OFDM [23], multiple-input-multiple-output (MIMO), non-orthogonal multiple access (NOMA), etc. Considering these factors, the IEEE 802.15.7 task group [9] suggested the use of VOOK [25] and VPPM [26], to support dimming in the two types of physical (PHY) layers, PHY-I and PHY-II. As such, it is crucial to study the power spectral densities (PSDs) and determine the BW requirement of these modulation schemes to ascertain their feasibility in practical scenarios (ref. Section III-A). However, to the best of our knowledge, none of the above works attempts to derive and study the PSDs of VOOK and VPPM, and hence obtain their BW requirements.

2) CHANNEL EQUALIZATION

Channel equalization is realized through equalizer filters which are broadly classified into two main categories: analog and digital. Analog equalizer filters are typically high-pass filters implemented on hardware using resistive and capacitive components. Recently [27]–[30], such filters have been experimentally demonstrated for capacity enhancement of VLC systems. However, these filters suffer from two major drawbacks. Firstly, they introduce a form of ISI known as baseline wander, resulting in an exponential power penalty around the low-frequency region [31]. This renders analog equalizer filters unsuitable for dimming-based modulation techniques because these schemes have strong frequency components near the DC region. Secondly, it is difficult to quickly change the characteristics of the hardware filters to match the quasi-static channel conditions in indoor VLC systems. Hence, for channel equalization in dimmable VLC systems, it is advisable to opt for digital equalizer designs which are usually implemented through digital signaling processing algorithms in software.

Digital equalizer filters (DEFs) are realized through software implementations of digital techniques like signal processing, beamforming, precoding, channel estimation, channel equalization, signal decoding etc. The DEFs used in VLC are required to have significantly different functionalities as compared to the DEFs used in conventional radio frequency communication (RFC) systems. The main reason behind this is the difference in channel conditions. While the channel in RFC systems is very dynamic, it is largely quasi-static in indoor VLC systems. Moreover, since VLC systems are designed to provide illumination along with communication, so certain functionalities like dimming, flickering, DC biasing, etc. are unique to VLC and are not required in RFC systems.

DEFs have been popularly used in MIMO-VLC systems for various functionalities [32]–[37]. Authors in [32] and [33] employ DEFs in MIMO decoding and in successive interference cancellation (SIC) for NOMA, respectively. They analyze and compare the performance of different types of DEFs in MIMO-VLC systems. In [34] and [35], authors attempt to maximize the achievable sum rate by using beamforming techniques and neural network-based equalization, respectively, in a multiuser MIMO-VLC system. The studies in [36], [37] and [38] explore DEF-based precoding techniques for performance enhancement of multiuser MIMO-VLC and NOMA-VLC systems, respectively.

Authors in [39], [40] investigate the use of DEFs for channel estimation in VLC systems. While [39] uses the least squares and the minimum mean square error (MMSE) algorithms for channel estimation in an OFDM-VLC system, [40] proposes an adaptive statistical Bayesian MMSE technique for optical OFDM aided VLC systems. However, except [35] and some other sporadic attempts [41]–[44], not much research has been done to mitigate ISI in VLC systems by implementing DEFs. In [41], feed-forward pre-equalization is used to mitigate ISI and achieve multi-gigabit transmission over VLC channels. Authors in [42] use adaptive nonlinear equalization by combining sparse Bayesian learning and Kalman filtering for VLC. Frequency domain equalization and fractionally spaced equalization are proposed in [43] and [44], respectively, for the performance enhancement of VLC systems.

ZFE is the simplest DEF, and its applications have been investigated in some of the above works [32]–[34], [38]. However, its use for ISI mitigation is not explored in the literature available on VLC. Recently, in [45], authors investigate different precoding and equalization schemes (including ZFE) for a 2×2 MIMO in a vehicle-to-vehicle VLC system, but this work is significantly different from ours. Firstly, and most importantly, the system under consideration in [45] is an outdoor VLC system while we consider an indoor scenario. Secondly, although the authors in [45] restrict the transmitted power to meet the dimming and illumination requirements, but there is no study on the effects of dimming on the error performance. Thirdly, they do not derive or study the spectral performance of dimming-based modulation schemes. Fourthly, they do not formulate the analytical model for the bit error rate (BER) of dimmable VLC systems with channel equalization.

ISI mitigation can also be achieved by using OFDM that distributes data onto different frequencies, thereby increasing the data's symbol time on each frequency. This is a very effective technique for frequency-selective channels. On the other hand, zero-forcing equalization can be used to invert the channel effects, particularly in slow fading channels (so that we can learn and adapt our equalizer). Many authors [46]–[48] have used zero-forcing equalization together with OFDM to invert any distortions on a single frequency. As this paper focuses on single carrier-based modulation schemes, we only discuss zero-forcing equalization.

Nevertheless, OFDM can be used over and above the ZFE approach for further improvements in data rates.

In summary, it is observed that one or more of the following aspects are not considered in the current state-of-the-art of dimming-based modulation schemes. Firstly, all of them lack a comprehensive analysis of the spectral performance of VOOK and VPPM, which have been suggested in the IEEE 802.15.7 standard [8], [9]. Secondly, a clear and complete formulation of their error performance is often missing. Thirdly, none of the existing works on equalizer filters in VLC considers the aspect of dimming control. Fourthly, and most importantly, there has been no attempt to mitigate ISI using channel equalization in dimmable VLC systems.

B. CONTRIBUTIONS

Motivated by the observations mentioned above, we attempt to bridge these gaps in the existing literature on dimming-based modulation schemes in VLC. Our work aims to study, improve, and integrate both aspects of the dual-functionality applications envisioned for VLC, i.e., illumination with dimming control and reliable data transmission with superior error performance. We present a comprehensive quantitative study on the spectral analysis and error performance of VOOK and VPPM schemes that enable dimming control. To the best of our knowledge, there is no existing work that studies channel equalization to mitigate ISI and ameliorate the error performance of VLC systems that are based on dimming-based modulation schemes. The key novel contributions of our work are as follows.

1) We formulate and study the PSDs of VOOK and VPPM and highlight the effect of dimming on their spectral performance.
2) We compare the different types of definitions used to quantify the BW requirement and determine the most precise definition that can be used for reliable implementation of practical dimmable VLC systems.
3) We implement ZFE for ISI mitigation in a dimmable VLC system and formulate the analytical model for the same.
4) Using Gram-Schmidt orthogonalization and vector space analysis of signals, we derive the expressions for the BER of a VLC system that employs dimming-based modulation schemes like VOOK and VPPM.
5) We study the effect of changing the dimming levels and increasing the data rate on the error performance of dimmable VLC systems.
6) At different data rates, we compute the power savings achieved by mitigating ISI using channel equalization. This is calculated as the difference in power levels required to maintain the same BER with and without equalization.
7) We determine the data rate beyond which the implementation of ZFE is advantageous, i.e., when the effect of ISI is more significant as compared to that of noise enhancement.

The remainder of this paper is organized as follows. We describe the dimming-based modulation schemes in Section II and analyze their spectral performance in Section III. We present the system model in Section IV and formulate the analytical model for ISI mitigation using ZFE in Section V. We discuss and analyze the error performance of the system in Section VI. Finally, we give a brief conclusion of work in Section VII.

II. DIMMING-BASED MODULATION SCHEMES

In this section, we describe the two dimming-based modulation schemes popularly used in VLC to control the brightness level of the emitted light. The brightness level is quantified by the dimming factor (γ), which is defined as the ratio of average optical power (P_γ) at that brightness level and the average optical power (P_f) under full brightness, i.e., $\gamma = P_\gamma / P_f$ [20]. Hence, $\gamma = 0$ indicates that the LED is completely switched off, whereas $\gamma = 1$ denotes that the LED is switched on at full brightness. Since LEDs are current-driven devices, their brightness is proportional to the input current and, hence, dimming control is achieved by varying the forward input current. There are two primary approaches to control the average current flowing through the LEDs [49].

The first approach is called amplitude modulated (AM) dimming in which the peak current or amplitude of the current pulses is varied to control the average input current. This method is cost-effective and simple, but continuously changing the current amplitude can create several problems, which render AM dimming unsuitable for practical implementation. Firstly, rapid changes in the peak current affect the wavelength (and hence, the color) of the emitted light leading to the problem of chromatic shift [50]. For example, the peak wavelengths of red LEDs (AlGaInP) shift towards shorter wavelengths, while those of the green and blue LEDs (InGaN) shift towards longer wavelengths [51]. This undesired color shift is caused by the quasi-Fermi level moving away from the band edge as the injection current increases [50], and it adversely affects the illumination performance. Secondly, continuous adjustments to the input current reduce the energy efficiency of the driver circuits [52]. Thirdly, AM dimming causes non-linearities in the output characteristics of the digital-to-analog converters driving the LEDs [52]. Fourthly, it is often difficult to adjust the current amplitude precisely, i.e., fine-tuning the LED's brightness is not easy with AM dimming [20]. Due to these issues, amplitude dimming is not preferred for VLC.

The second approach is pulse-width modulated (PWM) dimming, in which the average current is controlled by varying the width of the input current pulses. In PWM dimming, the brightness level is determined by the proportion of the time the LEDs are kept in the ON state. This dimming method is inherently linear. We now describe the two PWM dimming-based modulation schemes mentioned in the IEEE 802.15.7 standard [8], [9] for short-range wireless optical communication using visible light.

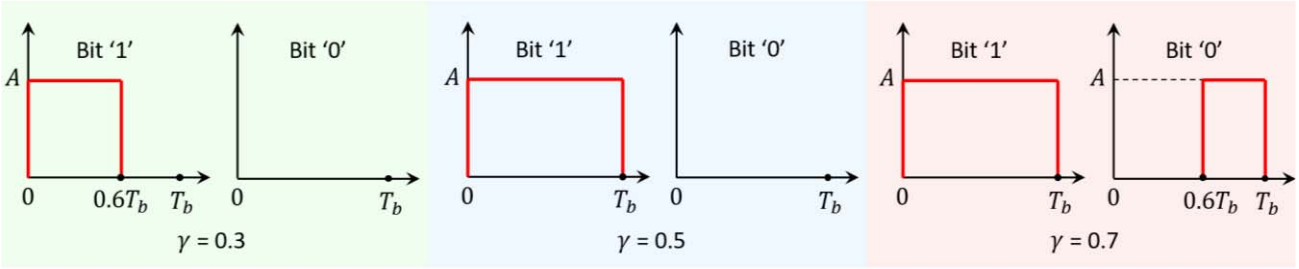

FIGURE 1. VOOK signal waveforms of bits '1' and '0' for different dimming levels (γ).

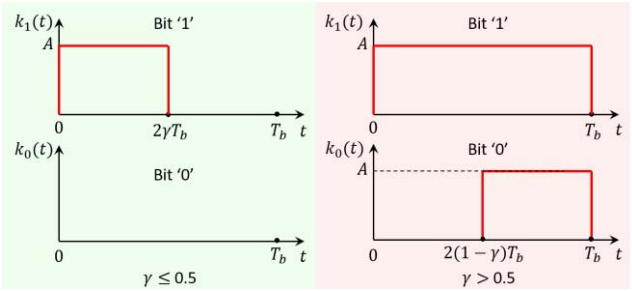

FIGURE 2. VOOK signal waveforms for any general dimming level (γ).

A. VARIABLE ON-OFF KEYING (VOOK)

VOOK is a hybrid combination of OOK and PWM, where OOK provides data communication, and PWM enables dimming control [25]. In Fig. 1, we depict the VOOK signal waveforms for bits '1' and '0' when $\gamma = 0.3$, $\gamma = 0.5$ and $\gamma = 0.7$, where we observe that at $\gamma = 0.5$, the VOOK signal waveforms are the same as those for OOK with non-return-to-zero (NRZ) pulses, i.e., a full pulse for the entire bit duration T_b for bit '1' and no pulse for bit '0'. When γ is reduced below 0.5, the LED remains off for bit '0', and the pulse width for bit '1' is decreased to reduce the average forward current. On the other hand, when γ is increased above 0.5, then the LED remains on for bit '1'and also during a small portion of T_b for bit '0', thereby increasing the average forward current and hence the LED brightness. Note that communication is not possible for $\gamma = 0$ and $\gamma = 1$. Based on the above discussion, we generalize and obtain the VOOK signal waveforms $k_1(t)$ and $k_0(t)$ for bits '1' and '0', respectively, at any general value of γ, as illustrated in Fig. 2. These are expressed mathematically as,

$$k_1(t) = \begin{cases} A\ \text{rect}\left(\frac{t}{2\gamma T_b} - \frac{1}{2}\right), & \gamma \leq 0.5 \\ A\ \text{rect}\left(\frac{t}{T_b} - \frac{1}{2}\right), & \gamma > 0.5, \end{cases} \tag{1}$$

and,

$$k_0(t) = \begin{cases} 0, & \gamma \leq 0.5 \\ A\ \text{rect}\left(\frac{t}{(2\gamma-1)T_b} - \frac{3-2\gamma}{4\gamma-2}\right), & \gamma > 0.5, \end{cases} \tag{2}$$

where A is the signal amplitude and rect(x) is the rectangular function defined as,

$$\text{rect}(x) = \begin{cases} 1, & |x| \leq \frac{1}{2} \\ 0, & \text{otherwise.} \end{cases} \tag{3}$$

Using Fig. 2, we also obtain the duration of the smallest pulse transition in VOOK signals which is expressed as,

$$T_{c,\text{K}} = \begin{cases} 2\gamma T_b, & \gamma \leq 0.5 \\ 2(1-\gamma)T_b, & \gamma > 0.5. \end{cases} \tag{4}$$

Note that, for $\gamma \leq 0.5$, the smallest transition is a 0-1-0 transition whereas for $\gamma > 0.5$, it is a 1-0-1 transition.

B. VARIABLE PULSE POSITION MODULATION (VPPM)

By changing the pulse-widths, binary pulse position modulation (2-PPM) is modified to VPPM to incorporate the dimming control feature [9]. Hence, VPPM is inherently a combination of 2-PPM and PWM, such that data communication is obtained by 2-PPM whereas dimming control is achieved by PWM. The signal waveforms for different dimming levels of VPPM are depicted in Fig. 3. It is evident from these figures that at $\gamma = 0.5$, VPPM transforms into 2-PPM with NRZ pulses. To reduce dimming below 0.5, we decrease the width of both the pulses without affecting their positions. This reduces the average forward current and, consequently, the brightness of the LEDs. Similarly, we increase the pulse width for both bits to increase the dimming level above 0.5, thereby enhancing the LED forward current and their brightness. Note that, like VOOK, communication is not possible for $\gamma = 0$ and $\gamma = 1$ in VPPM as well. Using these observations, we generalize to express the VPPM signal waveforms $p_1(t)$ and $p_0(t)$ for bits '1' and '0', respectively, at any general value of γ, as depicted in Fig. 4. These are expressed mathematically as given below:

$$p_1(t) = A\ \text{rect}\left(\frac{t}{\gamma T_b} - \frac{2-\gamma}{2\gamma}\right), \tag{5}$$

and,

$$p_0(t) = A\ \text{rect}\left(\frac{t}{\gamma T_b} - \frac{1}{2}\right). \tag{6}$$

From Fig. 4, we also observe and express the duration of the smallest pulse transition in VPPM signals as,

$$T_{c,\text{P}} = \begin{cases} \gamma T_b, & \gamma \leq 0.5 \\ (1-\gamma)T_b, & \gamma > 0.5. \end{cases} \tag{7}$$

Like VOOK, it should be noted that for VPPM also, the smallest transition is a 0-1-0 transition when $\gamma \leq 0.5$, and it is a 1-0-1 transition for $\gamma > 0.5$.

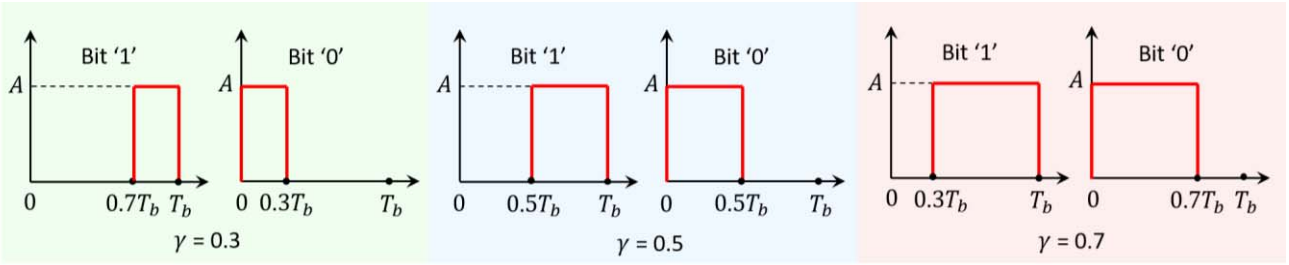

FIGURE 3. VPPM signal waveforms of bits '1' and '0' for different dimming levels (γ).

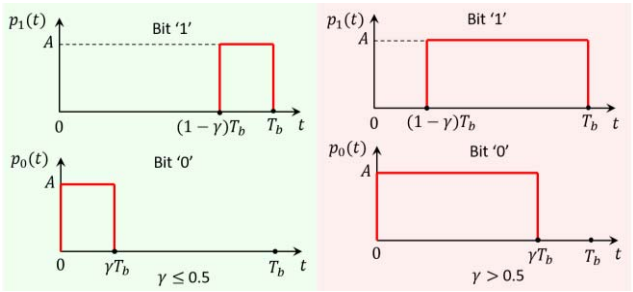

FIGURE 4. VPPM signal waveforms for any general dimming level (γ).

III. SPECTRAL ANALYSIS

In this section, we analyze the spectral performance of the dimming-based modulation schemes in terms of their PSD and hence obtain the BW required by these modulation schemes.

A. POWER SPECTRAL DENSITY (PSD)

The PSD of a signal is its power spectrum, depicting the distribution of power as a function of frequency. The PSD of the transmitted signal plays a crucial role in the design of communication systems due to several reasons. Firstly, it gives a foresight regarding the effect that the transmission channel might have on the propagating signals, leading to the discussion on the BW required by these signals. Secondly, in multiuser systems, analyzing the PSD helps in anticipating the amount of inter-user interference due to spectral overlap between adjacent channels (also known as crosstalk). Thirdly, a knowledge of the signals' PSD helps in ensuring that the constraints imposed by the regulatory bodies are satisfied. Hence, it is crucial to study the PSD of the signals generated by the dimming-based modulation schemes that have been recently proposed for VLC.

Note that these schemes use a different pulse shape for each symbol, so they are non-linear modulation schemes. Moreover, in a practical communication system, the sample functions of a binary information stream are not deterministic, and not of finite energy. So, the simple approach of calculating PSD as the time average of the energy spectral density is not valid for such schemes. However, in such cases, the auto-correlation function (ACF) can be obtained using the statistical properties, and the Fourier transform of the ACF gives the PSD of the signal.

We now briefly describe the derivation of PSD of an L-ary modulation scheme which is considered to be non-linear for the sake of generality. During each symbol period (T_s), the modulator present in this communication system produces one of the L signal waveforms depending upon the input bit sequence $\{x_n\}$. In general, the signals have arbitrary shapes and are not selected independently, e.g., when $\{x_n\}$ is coded prior to modulation, either for error control or spectrum shaping or both. The output of the modulator is modeled as a random process formed by the temporal superposition of all signals, and each of these L signals is a sample function from this random process. Hence, the modulator output is expressed as,

$$s(t) = \sum_{n=-\infty}^{\infty} s_{x_n}(t - nT_s). \tag{8}$$

The above signal lacks randomization of the timing epoch and is not a wide-sense stationary random process. Rather, it is a cyclostationary random process, and its mean and ACF are periodic functions of time. The mean and ACF for such processes are calculated by averaging over the time period which is T_s in this case. The desired PSD of the signal is obtained by taking the Fourier transform of the ACF, and is expressed as shown in (9) at the bottom of the page [53]. Here $\mathbb{P}(i)$ is the marginal probability of the i^{th} signal $s_i(t)$, $\delta(.)$ is the Dirac delta function, $S_i(f)$ is the Fourier transform of $s_i(t)$, and $\mathbb{P}_m(k|i)$ is the probability that $s_k(t)$ is transmitted m symbol periods after the transmission of $s_i(t)$. In (9), we observe that the first term represents the discrete component $Z_{\mathrm{d,s}}(f)$ of the PSD, comprising of possible spectral lines arising due to the periodicities in the

$$Z_{\mathrm{s}}(f) = \frac{1}{T_s^2}\sum_{n=-\infty}^{\infty}\left|\sum_{i=0}^{L-1}\mathbb{P}(i)S_i\left(\frac{n}{T_s}\right)\right|^2\delta\left(f-\frac{n}{T_s}\right) + \frac{1}{T_s}\sum_{i=0}^{L-1}\sum_{k=0}^{L-1}\mathbb{P}(i)S_i(f)S_k^*(f)\left[\sum_{m=-\infty}^{\infty}\{\mathbb{P}_m(k|i)-\mathbb{P}(k)\}e^{-j2\pi fmT_s}\right] \tag{9}$$

ACF, whereas the second term denotes the continuous part $Z_{c,s}(f)$ of the PSD. Hence,

$$Z_s(f) = Z_{d,s}(f) + Z_{c,s}(f). \tag{10}$$

The spectral lines which make up the discrete component of the PSD can be used for the recovery of carrier frequency during phase demodulation or clock recovery for receiver synchronization. However, they do not contain any useful information related to the message signal being transmitted over the communication channel, and hence, they are considered a waste of signal power. Moreover, the spectral concentration of power can be a source of strong narrow-band interference to other users.

We now simplify the PSD expression by imposing the condition that symbols are chosen independently. In that case, we have [53],

$$\mathbb{P}_m(k \mid i) = \begin{cases} 1, & m = 0 \\ \mathbb{P}(k), & m \neq 0, \end{cases} \tag{11}$$

and hence, the continuum PSD gets reduced to,

$$Z_{c,s}(f) = \frac{1}{T_s}\sum_{i=0}^{L-1}\mathbb{P}(i)|S_i(f)|^2 - \frac{1}{T_s}\left|\sum_{i=0}^{L-1}\mathbb{P}(i)S_i(f)\right|^2. \tag{12}$$

Hence, the complete PSD for an L-ary modulation scheme with independent signals is given by (13) as shown at the bottom of the page. Since both, VOOK and VPPM, are binary modulation schemes with equiprobable symbols so $T_s = T_b$, $L = 2$ and $\mathbb{P}(0) = \mathbb{P}(1) = 1/2$. Substituting these values, the discrete and continuum parts of the PSD, respectively, boil down to,

$$Z_{d,s}(f) = \frac{1}{4T_b^2}|S_0(f) + S_1(f)|^2 \sum_{n=-\infty}^{\infty}\delta\left(f - \frac{n}{T_b}\right), \tag{14}$$

and (15) given at the bottom of the page. Using (14) and (15) with the signal waveforms presented in Section II, we now obtain the PSDs for VOOK and VPPM.

1) PSD OF VOOK

From (1) and (2), the Fourier transforms of the VOOK signals for bits '1' and '0' are obtained, respectively, as

$$K_1(f) = \begin{cases} 2\gamma AT_b\text{sinc}\big(2\gamma fT_b\big)e^{-j2\pi f\gamma T_b}, & \gamma \leq 0.5 \\ AT_b\text{sinc}\big(fT_b\big)e^{-j\pi fT_b}, & \gamma > 0.5, \end{cases} \tag{16}$$

and (17) given at the bottom of the page. Substituting in (14) and (15), we get the continuous and discrete parts of the PSD as shown in (18) and (19), respectively, at the bottom of the page.

For simplicity and ease of illustration, we normalize these two quantities as $\overline{Z}_{c,K}(f) = Z_{c,K}(f)/A^2T_b$ and $\overline{Z}_{d,K}(f) = Z_{d,K}(f)/A^2$. In Fig. 5, we depict $\overline{Z}_{c,K}(f)$ for different dimming levels. We observe that the continuous part of the PSD for γ is the same as that for $1-\gamma$. Moreover, at all dimming levels, the continuous part of the PSD has a strong DC component and weaker side lobes. The discrete counterparts are illustrated in Fig. 6, where we make some interesting observations. Firstly, unlike the continuous part, the discrete parts of the PSD for γ is not the same as that for $1-\gamma$. Secondly, as γ is increased from 0.1 to 0.9, the power in the DC spectral line increases significantly ($\sim$ 80 times). Thirdly, the power in the non-DC spectral lines falls sharply as γ is increased up to 0.5. These lines disappear completely at $\gamma = 0.5$, after which they are negligibly small. This can also be concluded mathematically from the expression of $Z_{d,K}(f)$ for $\gamma = 0.5$ in (19), where the $\text{sinc}(fT_b)$ term is zero for all integral values of fT_b. Hence, when dimming is increased, there is an increase in DC power and diminution of spectral lines. Both these effects are detrimental to the practical implementation of this modulation scheme. While

$$Z_s(f) = \frac{1}{T_s^2}\left|\sum_{i=0}^{L-1}\mathbb{P}(i)S_i(f)\right|^2\sum_{n=-\infty}^{\infty}\delta\left(f - \frac{n}{T_s}\right) + \frac{1}{T_s}\left[\sum_{i=0}^{L-1}\mathbb{P}(i)|S_i(f)|^2 - \left|\sum_{i=0}^{L-1}\mathbb{P}(i)S_i(f)\right|^2\right] \tag{13}$$

$$Z_{c,s}(f) = \frac{1}{2T_b}\Big[|S_0(f)|^2 + |S_1(f)|^2\Big] - \frac{1}{4T_b}|S_0(f) + S_1(f)|^2 \tag{15}$$

$$K_0(f) = \begin{cases} 0, & \gamma \leq 0.5 \\ (2\gamma - 1)AT_b\text{sinc}\big[(2\gamma-1)fT_b\big]e^{-j\pi f(3-2\gamma)T_b}, & \gamma > 0.5 \end{cases} \tag{17}$$

$$Z_{c,K}(f) = \begin{cases} \gamma^2A^2T_b\text{sinc}^2\big(2\gamma fT_b\big), & \gamma \leq 0.5 \\ \frac{A^2T_b}{4}\big\{\text{sinc}^2\big(fT_b\big) + (2\gamma-1)^2\text{sinc}^2\big[(2\gamma-1)fT_b\big] \\ \quad - 2(2\gamma-1)\text{sinc}\big(fT_b\big)\text{sinc}\big[(2\gamma-1)fT_b\big]\cos\big[2\pi f(1-\gamma)T_b\big]\big\}, & \gamma > 0.5 \end{cases} \tag{18}$$

$$Z_{d,K}(f) = \begin{cases} \gamma^2A^2\text{sinc}^2\big(2\gamma fT_b\big)\sum_{n=-\infty}^{\infty}\delta\Big(f - \frac{n}{T_b}\Big), & \gamma \leq 0.5 \\ \frac{A^2}{4}\big\{\text{sinc}^2\big(fT_b\big) + (2\gamma-1)^2\text{sinc}^2\big[(2\gamma-1)fT_b\big] + 2(2\gamma-1)\text{sinc}\big(fT_b\big) \\ \text{sinc}\big[(2\gamma-1)fT_b\big]\cos\big[2\pi f(1-\gamma)T_b\big]\big\}\sum_{n=-\infty}^{\infty}\delta\Big(f - \frac{n}{T_b}\Big), & \gamma > 0.5 \end{cases} \tag{19}$$

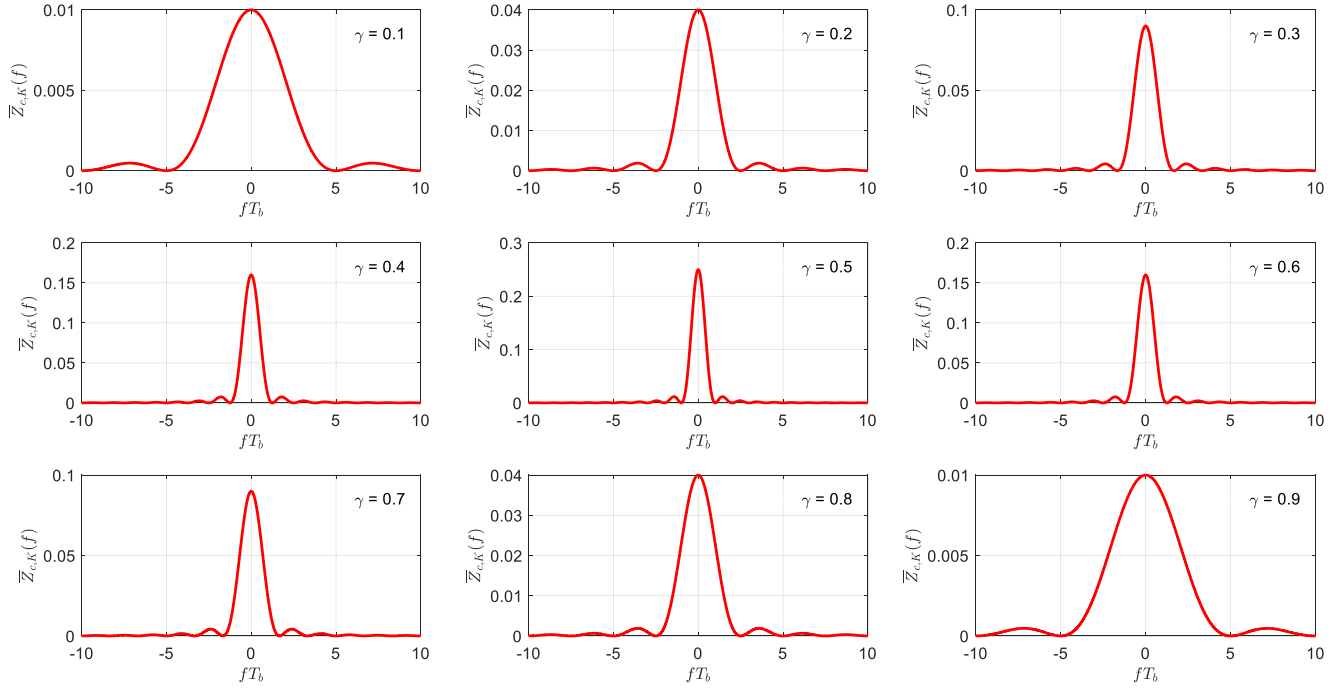

FIGURE 5. Normalized continuous part of the PSDs of VOOK at different dimming levels (γ).

a high value of DC power creates problems during AC coupling at the receiver, loss of non-DC spectral lines makes clock recovery difficult, especially for $\gamma \geq 0.5$.

2) PSD OF VPPM

Taking the Fourier transforms of the VPPM signals in (5) and (6), we get,

$$P_1(f) = \gamma A T_b \text{sinc}\big(\gamma f T_b\big) e^{-j\pi f(2-\gamma)T_b}, \tag{20}$$

and,

$$P_0(f) = \gamma A T_b \text{sinc}\big(\gamma f T_b\big) e^{-j\pi f \gamma T_b}. \tag{21}$$

Again, using (14) and (15), the PSD for VPPM is obtained as (22) given at the bottom of the page, and

$$Z_{\text{c,P}}(f) = \gamma^2 A^2 T_b \text{sinc}^2\big(\gamma f T_b\big) \sin^2\big[\pi f(1-\gamma)T_b\big]. \tag{23}$$

To analyze the spectral performance of VPPM, we now plot the normalized continuous and discrete parts of its PSD, i.e., $\overline{Z}_{\text{c,P}}(f) = Z_{\text{c,P}}(f)/A^2T_b$ and $\overline{Z}_{\text{d,P}}(f) = Z_{\text{d,P}}(f)/A^2$. In Fig. 7, we illustrate $\overline{Z}_{\text{c,P}}(f)$ for different dimming levels. Similar to that of VOOK, the continuous part of the PSD of VPPM is the same for γ and $1-\gamma$. However, unlike VOOK, there is no DC power in the continuous part of the PSD of VPPM. Another important observation is that the power content in the side lobes is very large at low and high values of γ and falls sharply as γ approaches 0.5. The discrete parts of VPPM's PSDs are depicted in Fig. 8, which are same as those of VOOK (ref. Fig. 6). This can be verified mathematically by observing the expressions of $Z_{\text{d,K}}(f)$ and $Z_{\text{d,P}}(f)$ in (19) and (22), respectively. We infer that, although they appear different, but using simple trigonometric manipulations, (19) can be simplified to (22) for integral values of n. Hence, similar to VOOK, VPPM also faces the problems of DC coupling and difficult clock recovery at high values of γ, i.e., for $\gamma \geq 0.5$.

B. BANDWIDTH REQUIREMENT

In the context of communication systems, the BW of a signal pertains to its spectral extent and is a quantitative measure of the frequency spectrum that a channel must provide for the faithful transmission of that signal. Without doubt, the BW requirement is a crucial parameter to gauge the suitability of a particular modulation format. However, unfortunately, since digital signals are time-limited, they have an infinite extent in frequency, and no physical communication channel can provide an infinite spectrum for transmission. Nevertheless, for most of these signals, it is possible to determine a range of frequencies in which most of the signal power is located. Based on the method adopted to determine this frequency range, there are three common definitions to measure the BW required by a communication signal [54]. Moreover, as discussed earlier, the discrete part of the PSD does not contain

$$Z_{\text{d,P}}(f) = \gamma^2 A^2 \text{sinc}^2\big(\gamma f T_b\big) \cos^2\big[\pi f(1-\gamma)T_b\big] \sum_{n=-\infty}^{\infty} \delta\left(f - \frac{n}{T_b}\right) \tag{22}$$

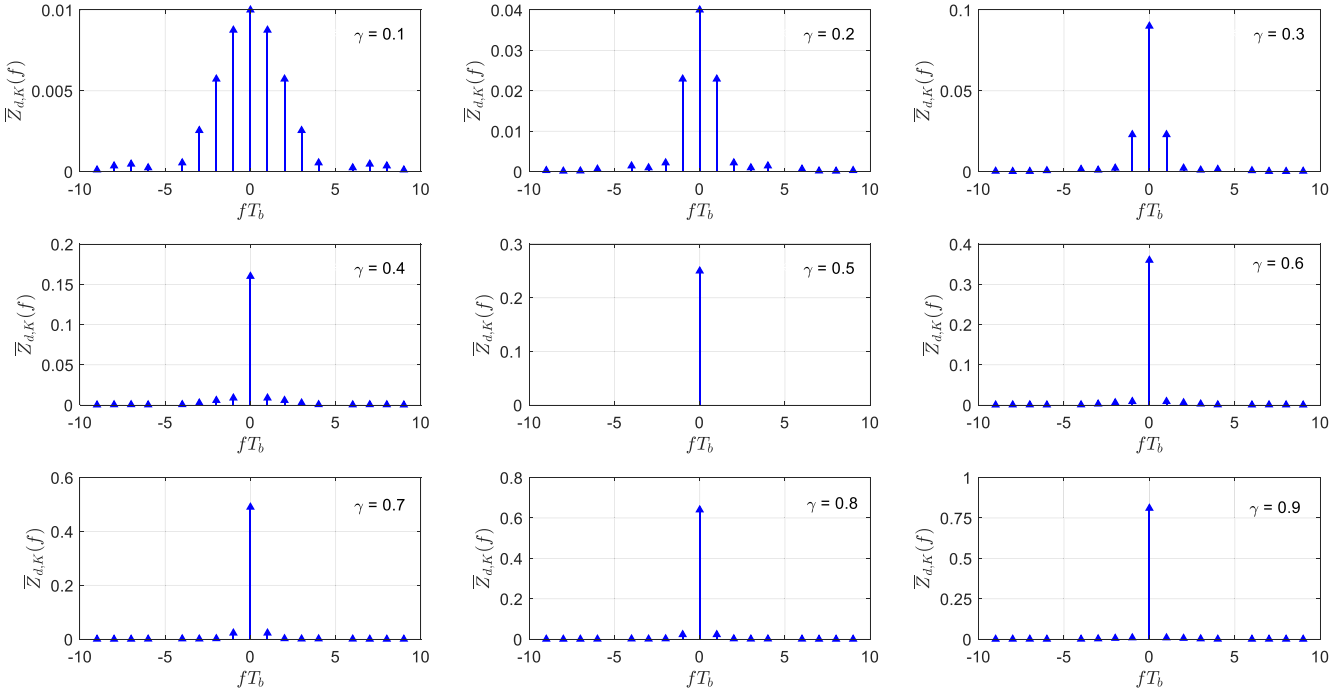

FIGURE 6. Normalized discrete part of the PSDs of VOOK at different dimming levels (γ).

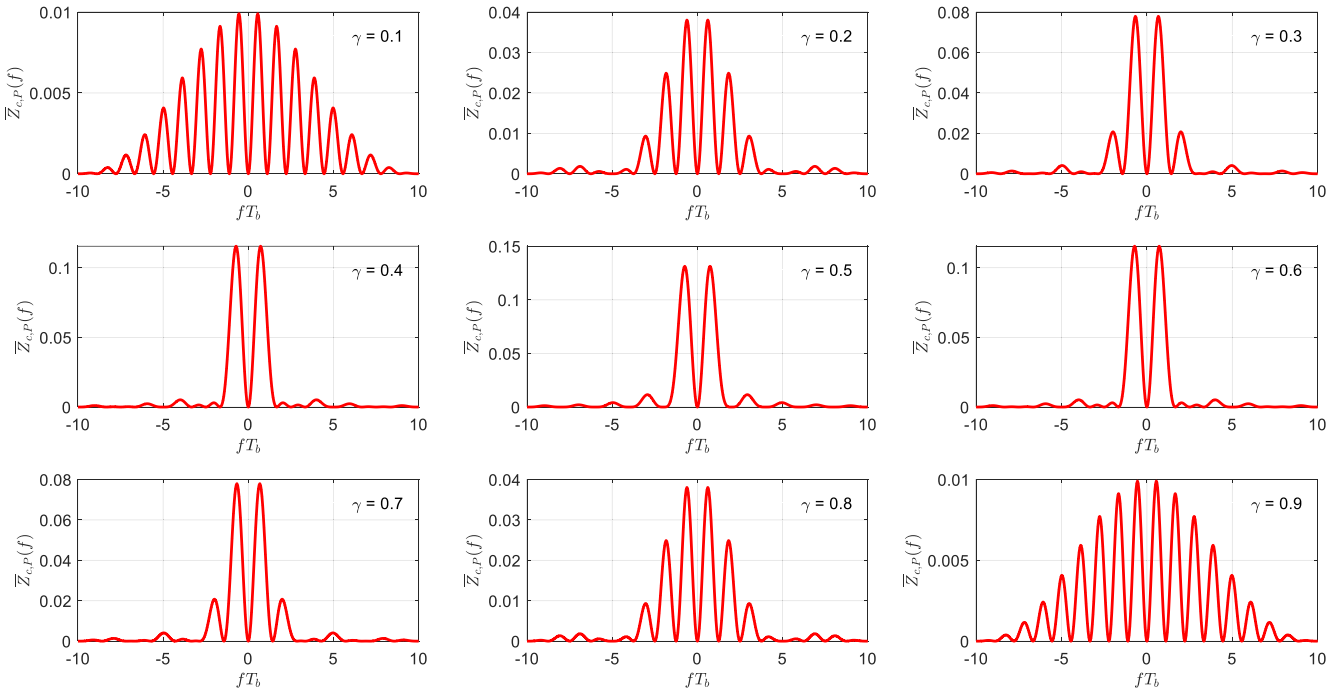

FIGURE 7. Normalized continuous part of the PSDs of VPPM at different dimming levels (γ).

any useful information of the message signal being transmitted, and hence, only the continuous part of the signal's PSD is used to calculate the BW required by that signal [53].

a) *Approximate BW:* In digital communication systems, the modulator output is a temporal superposition of time-limited signals. The more the signals are compressed in the time domain, the larger is the spectral spread. Hence, the approximate BW (B_a) is calculated as the inverse of the smallest temporal transition (T_c) present in the modulated signal as $B_a = 1/T_c$ [54]. It is based on the assumption that the smallest transition in time sets the upper limit on the spectral spread without considering other transitions. It is the simplest definition as it is calculated by merely observing

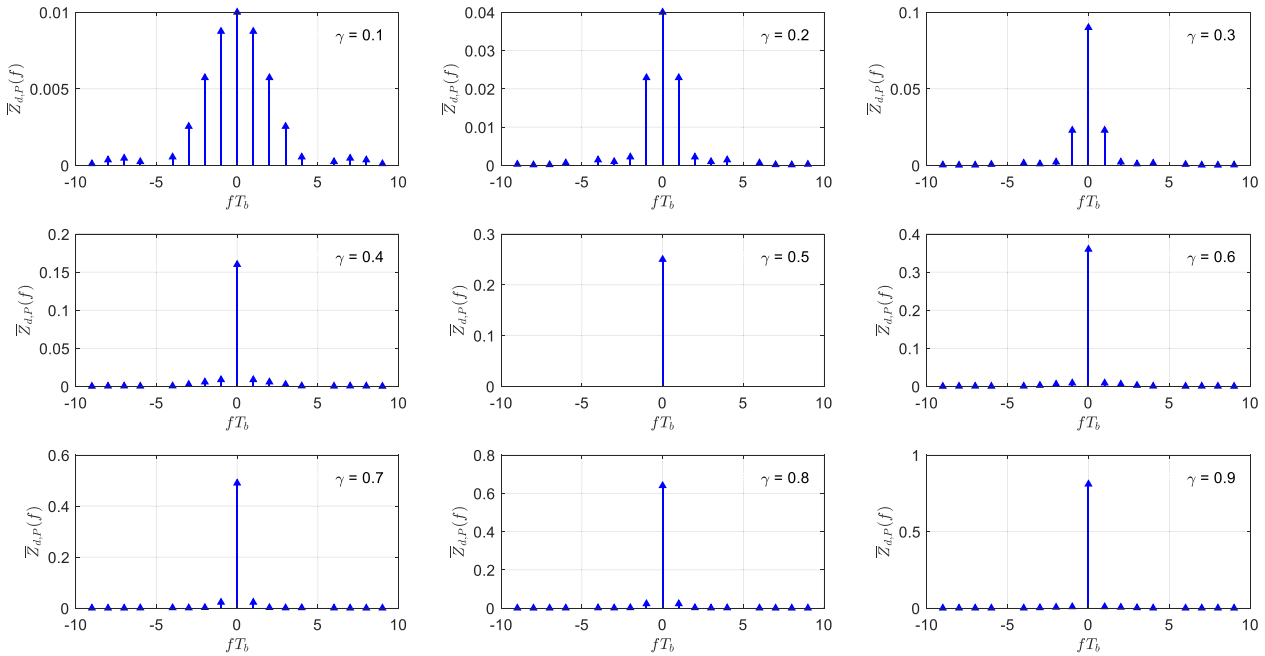

FIGURE 8. Normalized discrete part of the PSDs of VPPM at different dimming levels (γ).

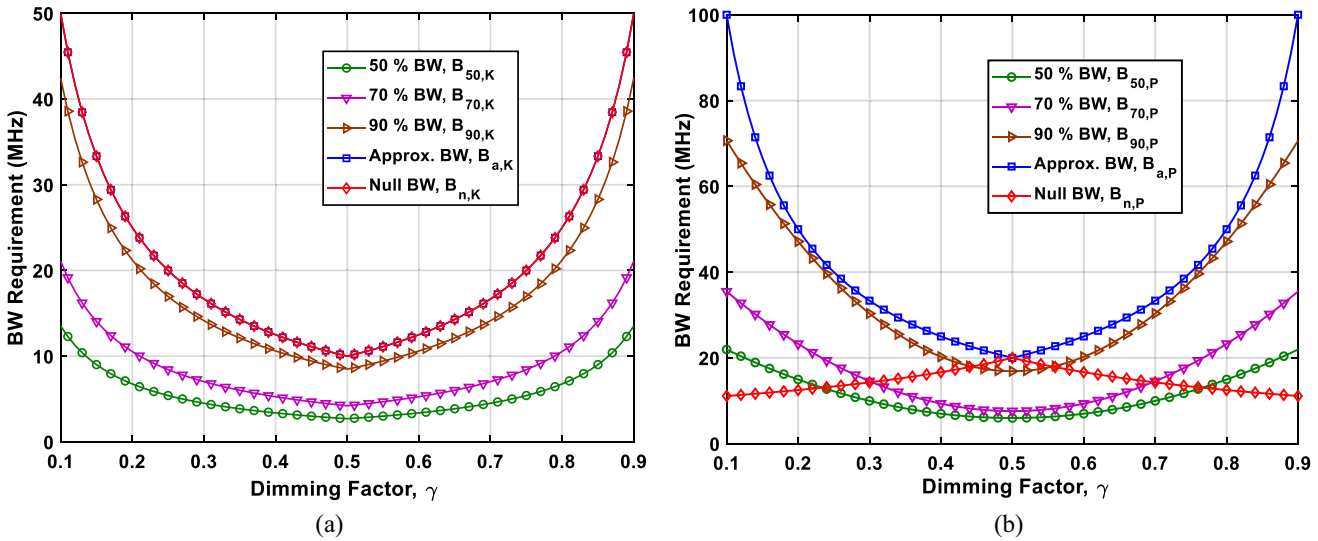

FIGURE 9. Approximate BW (B_a), first-null BW (B_n) and x % containment BW (B_x) required by (a) VOOK, and (b) VPPM with increase in dimming factor at bit rate, $R_b = 10$ Mbps. Here, subscripts K and P denote VOOK and VPPM, respectively.

the modulated signal waveform and does not require any knowledge of the signal's PSD. It provides a very reliable approximation of the BW when NRZ pulses are used for modulation.

b) *First-null BW:* First null BW (B_n) is the smallest non-DC frequency at which the PSD falls to null or zero [54]. It can be mathematically expressed as,

$$B_n = \min\{f_i : Z_{c,s}(f_i) = 0 \text{ and } f_i > 0\}. \tag{24}$$

This definition was developed keeping in view the lobed behavior of the PSD. It is based on the assumption that the PSD possesses a main spectral lobe containing most of the signal's power and bounded by well-defined spectral nulls. Since a graphical description of PSD suffices to calculate B_n, it is a simpler definition, but it lacks generality as it cannot be faithfully applied in modulation schemes where the signals do not have a lobed PSD with a prominent central lobe.

c) *Fractional Containment BW:* This definition specifies the range of frequencies that contain a certain fraction (say x %) of the signal power [54]. It is calculated from the signal's PSD as $B_x = f_1$ such that the following condition holds:

$$\int_0^{f_1} Z_{c,s}(f)\ df = \frac{x}{100} \times \int_0^{\infty} Z_{c,s}(f)\ df. \tag{25}$$

It is the most precise definition of BW since it measures the power without making any assumptions. However, it requires the complete knowledge of the mathematical expression of the signal's PSD and the ability to integrate the same mathematically.

We now calculate the BW required by VOOK and VPPM at different dimming levels, and compare the results obtained using the three definitions explained above.

1) BW REQUIREMENT OF VOOK

The approximate BW of VOOK is calculated as the reciprocal of $T_{c,\mathrm{K}}$ given in (4), to get

$$B_{a,\mathrm{K}} = \begin{cases} \frac{R_b}{2\gamma}, & \gamma \leq 0.5 \\ \frac{R_b}{2(1-\gamma)}, & \gamma > 0.5, \end{cases} \tag{26}$$

where $R_b = 1/T_b$ is the bit rate of data transmission.

To obtain the first-null BW, we need to find the null positions in the continuous part of VOOK's PSD $Z_{\mathrm{c,K}}(f)$ depicted in (18). For $\gamma \leq 0.5$, the spectral nulls occur when $2\gamma f T_b = n_1 \ \forall \ n_1 \in \mathbb{I}^+$ where $\mathbb{I}^+$ is the set of positive integers. The first-null is obtained when $n_1 = 1$. Similarly, for $\gamma > 0.5$, the spectral nulls occur when $\mathrm{sinc}(fT_b) = -(2\gamma - 1)\mathrm{sinc}[(2\gamma - 1)fT_b]$ and $\cos[2\pi f(1-\gamma)T_b] = -1$. The first condition mandates that $fT_b = fT_b(2\gamma - 1) + (2n_2 - 1) \ \forall \ n_2 \in \mathbb{I}^+$ while the second condition boils down to $2\pi f(1-\gamma)T_b = (2n_3 - 1)\pi \ \forall \ n_3 \in \mathbb{I}^+$. The first-null is obtained when $n_2 = n_3 = 1$ at which both conditions are satisfied simultaneously for the same value of frequency. Hence, we get

$$B_{n,\mathrm{K}} = \begin{cases} \frac{R_b}{2\gamma}, & \gamma \leq 0.5 \\ \frac{R_b}{2(1-\gamma)}, & \gamma > 0.5. \end{cases} \tag{27}$$

Using (25), we also calculate the fractional containment BWs, $B_{50,\mathrm{K}}$, $B_{70,\mathrm{K}}$ and $B_{90,\mathrm{K}}$. In Fig. 9(a), we plot the BW requirement of VOOK with an increase in dimming level for $R_b = 10$ Mbps. We observe that when γ is increased from 0.1 to 0.5, the width of the smallest pulse transition in the signal waveform increases (ref. Figs. 1 and 2), and hence, the BW requirement gets reduced. However, when γ is increased beyond 0.5 up to 0.9, the required BW increases due to a reduction in the width of the smallest pulse transitions. Consequently, the BW curves are symmetric about $\gamma = 0.5$, which is expected because the continuous PSDs used to calculate the BW are the same for γ and $1-\gamma$ (ref. Fig. 5). Moreover, $B_{50,\mathrm{K}} < B_{70,\mathrm{K}} < B_{90,\mathrm{K}}$ because more BW is required to transmit a higher fraction of the signal power faithfully. Furthermore, $B_{a,\mathrm{K}} = B_{n,\mathrm{K}}$, so the plots of $B_{a,\mathrm{K}}$ and $B_{n,\mathrm{K}}$ overlap.

2) BW REQUIREMENT OF VPPM

To obtain the approximate BW of VPPM, we take the inverse of $T_{c,\mathrm{P}}$ expressed in (7), to get,

$$B_{a,\mathrm{P}} = \begin{cases} \frac{R_b}{\gamma}, & \gamma \leq 0.5 \\ \frac{R_b}{(1-\gamma)}, & \gamma > 0.5. \end{cases} \tag{28}$$

We now compute the first-null BW by locating the null positions in $Z_{\mathrm{c,P}}(f)$ as given in (23). Spectral nulls occur when either $\gamma f T_b = n_4 \ \forall \ n_4 \in \mathbb{I}^+$ or $\pi f(1-\gamma)T_b = n_5\pi \ \forall \ n_5 \in \mathbb{I}^+$. The first-null is obtained when $n_4 = n_5 = 1$. Invoking the minimum condition of (24), we get

$$B_{n,\mathrm{P}} = \begin{cases} \frac{R_b}{(1-\gamma)}, & \gamma \leq 0.5 \\ \frac{R_b}{\gamma}, & \gamma > 0.5. \end{cases} \tag{29}$$

We also calculate the fractional containment BWs, $B_{x,\mathrm{P}}$ for $x = 50$, 70, and 90. In Fig. 9(b), with $R_b = 10$ Mbps, we depict the BW required by VPPM with an increase in dimming level. Similar to VOOK, and for the same reasons (ref. Figs. 3, 4 and 7), the BW curves are symmetric about $\gamma = 0.5$. We also observe that $B_{50,\mathrm{P}} < B_{70,\mathrm{P}} < B_{90,\mathrm{P}}$ because more BW is required to transmit a higher fraction of the signal power faithfully. However, a very interesting and unique observation is that, for VPPM, $B_{a,\mathrm{P}} \neq B_{n,\mathrm{P}}$, except at $\gamma = 0.5$. The shape and trend of $B_{a,\mathrm{P}}$ agrees with $B_{x,\mathrm{P}}$ for $x = 50$, 70 and 90, and hence, $B_{a,\mathrm{P}}$ is sufficiently reliable. On the contrary, $B_{n,\mathrm{P}}$ gives a highly misleading estimate of the BW. The reason for the failure of $B_{n,\mathrm{P}}$ is the fact that, for $\gamma \neq 0.5$, the PSDs of VPPM do not contain a prominent central spectral lobe (ref. Fig. 7). As γ deviates away from 0.5, the strength of the spectral lobes becomes more and more comparable to each other, and hence, neglecting the power contained in the side lobes leads to erroneous results. Therefore, first-null BW fails to estimate the BW requirement in case of VPPM correctly.

Evidently, for both schemes, the approximate BW, B_a gives a very reliable estimate of the BW requirement. It is, therefore, used to calculate the spectral efficiency of the modulation schemes as $\mu = R_b/B_a$. Substituting (26) and (28), we get the spectral efficiencies of the two schemes as,

$$\mu_{\mathrm{K}} = \begin{cases} 2\gamma, & \gamma \leq 0.5 \\ 2(1-\gamma), & \gamma > 0.5, \end{cases} \tag{30}$$

and,

$$\mu_{\mathrm{P}} = \begin{cases} \gamma, & \gamma \leq 0.5 \\ (1-\gamma), & \gamma > 0.5. \end{cases} \tag{31}$$

Hence, VOOK is twice as spectrally efficient as VPPM. This is also evident in Fig. 10, where the spectral efficiencies of both the schemes are plotted for comparison.

IV. SYSTEM MODEL

In this section, we present the system model used in our work. We describe the multipath VLC channel model and the indoor configuration simulated in our study.

A. MULTIPATH CHANNEL MODEL

In VLC, data is transmitted over visible light signals. While propagating from the LED transmitters to photodiode receivers, these signals travel via multiple paths (ref. Fig. 11) due to reflections occurring at the walls of the indoor environment. The reflections are mostly diffused in nature, and hence, can be modeled using the Lambertian radiation

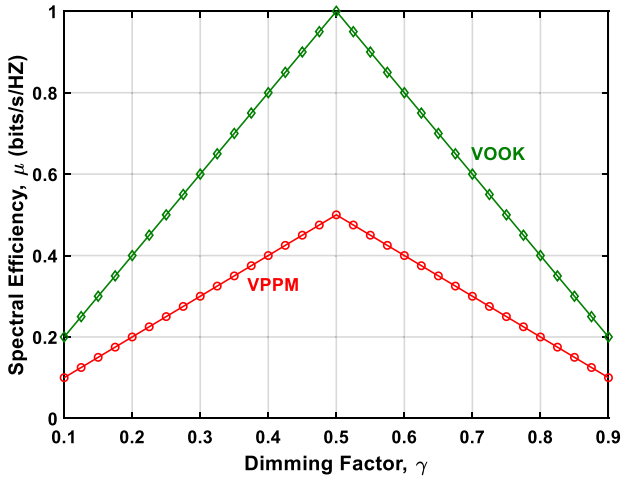

FIGURE 10. Variation of spectral efficiency with increase in dimming factor for VOOK and VPPPM.

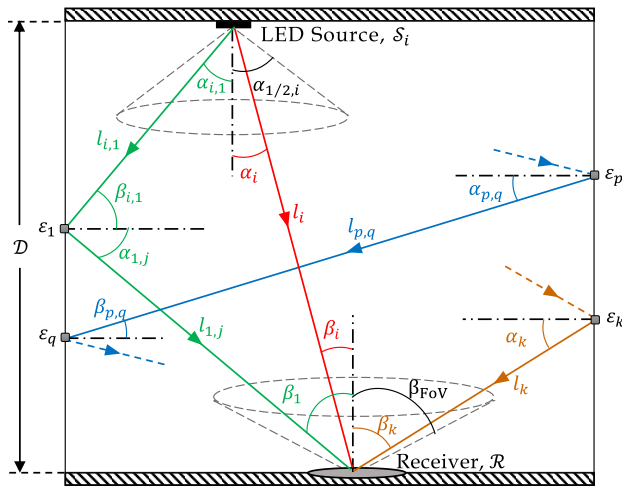

FIGURE 11. Depiction of the multipath propagation of light signals in a VLC channel.

model [55]. The multipath propagation occurs via two types of paths. The first type is the line-of-sight (LoS) path which is a direct path between the transmitter and receiver. The second type comprises non-line-of-sight (NLoS) paths which are circuitous paths including at least one reflection [56]. Due to the multipath propagation of visible light signals, the received optical signal in the indoor VLC link experiences time dispersion leading to ISI. The multipath channel model for indoor VLC systems is explained in great detail in [55], where the channel impulse response between the i^{th} source $\mathcal{S}_i$ and the receiver $\mathcal{R}$ is derived to be,

$$h(t) = \sum_{i=1}^{N_P} \left[h_i^{(0)}(t; \mathcal{S}_i, \mathcal{R}) + \sum_{k=1}^{K} h_i^{(k)}(t; \mathcal{S}_i, \mathcal{R}) \right], \quad (32)$$

where K is the reflection order defined as the total number of reflections modeled in the system, N_P is the total number of LED panels, and $h_i^{(0)}(t; \mathcal{S}_i, \mathcal{R})$ and $h_i^{(k)}(t; \mathcal{S}_i, \mathcal{R})$ are the impulse responses [55] of the LoS path and NLoS paths, respectively, as shown in (33) and (34) at the bottom of the page. The various physical parameters are depicted in Fig. 11, where $\mathcal{D}$ is the vertical separation between the transmitter and receiver planes, l_i is the path length between $\mathcal{S}_i$ and $\mathcal{R}$, $\mathcal{A}_\mathcal{R}$ is the physical area of the receiving element $\mathcal{R}$, α_i is the angle of irradiance from $\mathcal{S}_i$ to $\mathcal{R}$, β_i is the angle of incidence at $\mathcal{R}$, $\delta(.)$ is the Dirac delta function, T_f is the transmission coefficient of the optical filter, c is the velocity of light, β_{FoV} is the field of view (FoV) of $\mathcal{R}$, N_R is the total number of reflective elements, ρ_r is the reflection coefficient of the r^{th} reflective element ε_r, $l_{i,r}$ is the path length between $\mathcal{S}_i$ and ε_r, $\alpha_{i,r}$ is the angle of irradiance from $\mathcal{S}_i$ to ε_r, $\beta_{i,r}$ is the angle of incidence at ε_r, $\mathcal{A}_{\varepsilon_r}$ is the physical area of ε_r, and m_i is the Lambertian order of radiation of the source $\mathcal{S}_i$, defined as [56],

$$m_i = \frac{-\ln 2}{\ln(\cos \alpha_{1/2,i})}, \quad (35)$$

where $\alpha_{1/2,i}$ is the semi-angle of the LED source $\mathcal{S}_i$. Moreover, $g_c(\beta)$ is the gain of the optical concentrator at the receiver given as [57],

$$g_c(\beta) = \begin{cases} \frac{\nu_c^2}{\sin^2 \beta_{\text{FoV}}}, & 0 \le \beta \le \beta_{\text{FoV}} \\ 0, & \beta > \beta_{\text{FoV}}, \end{cases} \quad (36)$$

where ν_c is the refractive index of the concentrator.

B. INDOOR CONFIGURATION

The indoor environment, as illustrated in Fig. 12, is a cuboidal room (5 m × 5 m × 3 m) with four LED panels installed symmetrically on the ceiling. Each LED panel, consisting of an equal number of identical LEDs, is considered as an abstract point source located at its center. This approximation is valid because the distance between any two adjacent LEDs on a panel is fixed at 1 cm, which is very small in comparison to the room width. Assuming a three-dimensional Cartesian system with its origin at the center of the room, the coordinates of the four LED panels ($\mathcal{S}_1$, $\mathcal{S}_2$, $\mathcal{S}_3$ and $\mathcal{S}_4$) are (−1.25, 1.25, 1.5), (1.25, 1.25, 1.5), (−1.25,

$$h_i^{(0)}(t; \mathcal{S}_i, \mathcal{R}) = \begin{cases} \frac{m_i+1}{2\pi l_i^2} \mathcal{A}_\mathcal{R} \cos^{m_i} \alpha_i \cos \beta_i \, g_c(\beta_i) T_f \delta\left(t - \frac{l_i}{c}\right), & 0 \le \beta_i \le \beta_{\text{FoV}} \\ 0, & \beta_i > \beta_{\text{FoV}} \end{cases} \quad (33)$$

$$h_i^{(k)}(t; \mathcal{S}_i, \mathcal{R}) = \begin{cases} \frac{m_i+1}{2\pi} \sum_{r=1}^{N_\text{R}} \frac{\mathcal{A}_{\varepsilon_r} \rho_r}{l_{i,r}^2} \cos^{m_i} \alpha_{i,r} \cos \beta_{i,r} \, h^{(k-1)}\left(t - \frac{l_{i,r}}{c}; \varepsilon_r, \mathcal{R}\right), & 0 \le \beta_{i,r} \le \frac{\pi}{2} \\ 0, & \beta_{i,r} > \frac{\pi}{2} \end{cases} \quad (34)$$

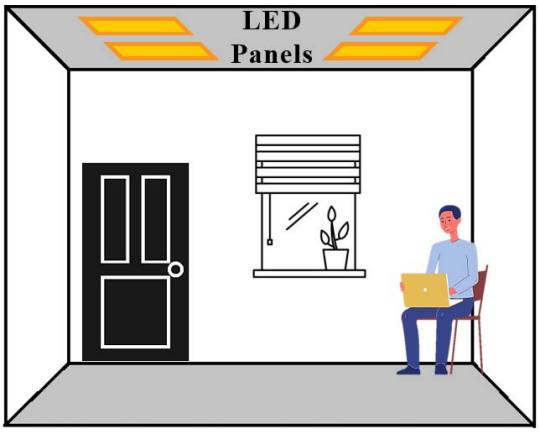

FIGURE 12. VLC indoor configuration depicting the four LED panels and the user.

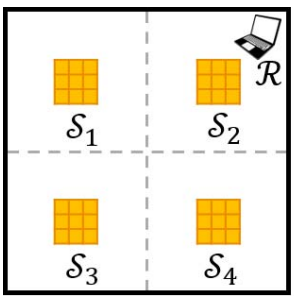

FIGURE 13. Illustration (top view) of the relative locations of the LED sources ($\mathcal{S}_1$, $\mathcal{S}_2$, $\mathcal{S}_3$, $\mathcal{S}_4$) on the ceiling and the fixed user ($\mathcal{R}$) located in the corner of the room.

-1.25, 1.5) and (1.25, -1.25, 1.5), respectively. The user with the photodiode receiver ($\mathcal{R}$) is located near the corner of the room, i.e., at (2, 2, -1.5). The user is assumed to be fixed and its location is chosen in order to study the worst-case BER performance [55]. The relative positions of the LED sources and the user is depicted in Fig. 13.

Visible light signals emanating from the LED sources undergo reflections (quantified by the reflection order, K) at the walls which are divided into reflective elements with the same reflectivity (ρ). It has been shown in [55], [56] that the multipath nature of the VLC channel can be adequately modeled with $K = 3$ and $\rho = 0.8$. After traversing the multipath VLC channel, the signals reach the photodiode receiver where noise is added to the received signal. In this work, we consider the white Gaussian noise with zero mean and variance of σ_{T}^2. The modeling of different components of this noise present in VLC is explained in [55], [58]. The values of the system parameters are summarized in Table 1.

In the system being studied in our paper, ISI in the wireless channel arises due to two main reasons. The first reason is the presence of multipath reflections in the VLC channel. Since visible light signals cannot penetrate through walls, so they undergo multiple successive reflections at these walls. These reflections create multiple paths from the LED source to the receiver, giving rise to the problem of delay spread because the light signals carrying the same data reach the receiver at

TABLE 1. System parameters.

Parameter	Value
Room size	5 m × 5 m × 3 m
Transmitter receiver separation, $\mathcal{D}$	2.15 m
Number of LED panels, N_p	4
Separation between two adjacent LEDs	1 cm
LED semi-angle, $\alpha_{1/2}$	60°
Physical area of photodetector, $\mathcal{A}_{\mathrm{PD}}$	1 cm^2
FoV of photodetector, β_{FoV}	85°
Responsivity of photodetector, $\Re$	0.8 A/W
Physical area of reflective wall elements, $\mathcal{A}_r$	0.04 m^2
Wall reflectivity, ρ	0.8
Reflection order, K	3
Transmission coefficient of filter, T_f	1
Refractive index of concentrator, ν_c	1.5
Line Coding	NRZ
Data Rate, R_b	650 Mb/s (variable)

different time instants. The second reason is the asymmetrical placement of LEDs. The illumination LEDs used for VLC have a non-directed diffuse radiation pattern and are installed in the form of panels on the ceiling [57]. So, the path lengths between each LED panel and the receiver are different. In such a system with a broadcasting scenario, where all LEDs transmit the same data, the presence of spatially distributed transmitters aggravates the delay spread. Hence, the presence of reflections and multiple transmitters creates the problem of delay spread, which is the primary reason for the origin of ISI in indoor VLC systems. In a typical indoor scenario (specifically a 5 m × 5 m × 3 m room, as considered in our study), the maximum values of root mean square (RMS) delay spread varies between 1 – 2.5 ns [55].

V. ISI MITIGATION USING CHANNEL EQUALIZATION

In this section, we implement a ZFE filter to achieve ISI mitigation. We analyze and derive the analytical expressions for BER when VOOK and VPPM are used as the modulation schemes. As explained in Section I, ISI affects all multipath wireless communication systems. The impulse response of a multipath VLC system with different transmitter-receiver configurations has been illustrated in several research works [59]–[67]. In [59]–[61], authors depict the impulse response for various relative locations of the transmitters and receivers, whereas authors in [62] vary the relative orientation of the transmitter and receiver and illustrate the corresponding impulse responses. Authors in [63], [64] study the impulse response for different spacings between LED transmitters. The effect of different types of reflections is investigated by plotting impulse responses of the VLC channel in [65], [66]. Recently, in [67], the impulse response of a multipath VLC system with 11 different transmitter configurations is studied in detail. In all these works [59]–[67], it is shown that, for all system configurations, the impulse response has a delay spread and hence, there is always ISI in the system. As such, in any realistic VLC system, the effect of ISI cannot be neglected without risking an overestimation of the results.

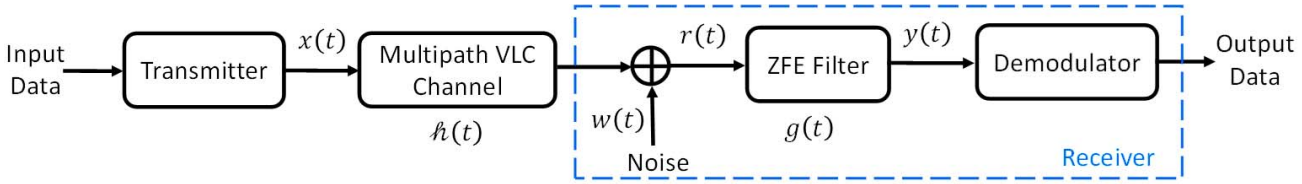

FIGURE 14. Simplified block diagram of a VLC system employing zero-forcing equalization (ZFE) for ISI mitigation.

A. ZERO-FORCING EQUALIZATION (ZFE)

Equalization aims to mitigate ISI by compensating for imperfections in the channel. In the simplest case, the equalizer filter has the inverse characteristics of the channel, essentially restoring the transmitted pulse shape at the receiver. Such a filter is known as the ZFE filter. A simplified block diagram of a VLC system employing a ZFE filter at the receiver is shown in Fig. 14. Here the transmitter block contains modulator, driver, and LEDs. The received signal is written as,

$$r(t) = \Re\big[x(t) * h(t)\big] + w(t), \tag{37}$$

where $x(t)$ is the transmitted signal, $*$ denotes the convolution operation, and $w(t)$ is the additive white Gaussian noise (AWGN) which is added at the photodetector and has a one-sided PSD of $\mathcal{N}_w$, such that $\mathcal{N}_w = 2\sigma_\Gamma^2$. Here, $h(t)$ is the impulse response of the multipath VLC channel as depicted in (32). For the sake of mathematical simplicity, it is expressed as,

$$h(t) = \sum_n \xi_n \delta\left(t - \frac{\mathcal{L}_n}{c}\right), \tag{38}$$

where ξ_n and $\mathcal{L}_n$ are the total loss and total length of the n^{th} path, respectively. If the signal component traversing the n^{th} path undergoes k reflections, then the n^{th} path comprises of $k+1$ segments between consecutive reflections, such that,

$$\xi_n = \rho^k \prod_{i=1}^{k+1} \zeta_{i,n} \quad \text{and,} \quad \mathcal{L}_n = \sum_{i=1}^{k+1} \ell_{i,n}, \tag{39}$$

where ρ is the wall reflectivity and $\zeta_{i,n}$ and $\ell_{i,n}$ are the path loss and path length, respectively, of the i^{th} segment of the n^{th} path [56]. Now, (37) is written in the frequency domain as,

$$R(f) = \Re X(f)H(f) + W(f), \tag{40}$$

where $R(f)$, $X(f)$, $H(f)$, and $W(f)$ are the Fourier transforms of $r(t)$, $x(t)$, $h(t)$ and $w(t)$, respectively. Hence, using (38), we get,

$$H(f) = \sum_n \xi_n \exp\left(-j2\pi f \frac{\mathcal{L}_n}{c}\right). \tag{41}$$

The output of the ZFE is,

$$Y(f) = R(f)G(f), \tag{42}$$

where $G(f)$ is the transfer function of the ZFE filter defined as [11],

$$G(f) = \frac{1}{H(f)}. \tag{43}$$

Hence, ZFE is a type of linear channel equalization technique which removes the channel distortions by completely inverting the channel response. It reduces the ISI to zero and hence its name. From (43), we have, $G(f)H(f) = 1$, which means that the combination of the ZFE filter and channel results in flat frequency response with zero phase. Using (40) – (43), we get,

$$Y(f) = \Re X(f) + N(f), \tag{44}$$

where $N(f) = W(f)/H(f)$ is the noise present in the ZFE output. Since physical channels are inherently lossy, $\max|H(f)| < 1$, and hence, although the ZFE filter eliminates the ISI due to channel effects, it leads to noise enhancement at the receiver. Therefore, the use of ZFE filer is advantageous when the effect of ISI is more significant as compared to the noise added by the detector [11]. The ZFE output is expressed in the time domain by taking the inverse Fourier transform of (44) as,

$$y(t) = \Re x(t) + n(t). \tag{45}$$

The PSD of $n(t)$ is obtained as,

$$\mathcal{N}_0 = \mathcal{N}_w |G(f)|^2. \tag{46}$$

Using (41), (43), and (46), we obtain,

$$\mathcal{N}_0 = \frac{\mathcal{N}_w}{\left|\sum_n \xi_n \exp\left(-j2\pi f \frac{\mathcal{L}_n}{c}\right)\right|^2}. \tag{47}$$

The maximum value of denominator in RHS of (47) is,

$$\left|\sum_n \xi_n \exp\left(-j2\pi f \frac{\mathcal{L}_n}{c}\right)\right|^2 \leq \sum_n \left(|\xi_n|^2 + 2\sum_{i<n} \xi_i \xi_n\right), \tag{48}$$

which results in a lower bound approximation of the error performance. From (47) and (48), we have,

$$\mathcal{N}_0 \geq \frac{\mathcal{N}_w}{\sum_n \left(|\xi_n|^2 + 2\sum_{i<n} \xi_i \xi_n\right)}. \tag{49}$$

B. BER EVALUATION

We use the Gram-Schmidt orthogonalization procedure (described briefly in the Appendix) to find the orthogonal representation of signals and find the Euclidean distance between them [68]. We summarize the steps to orthogonalize a binary set of signals $s_0(t)$ and $s_1(t)$ which can be represented as, $s_0(t) = s_{00}\phi_0(t) + s_{01}\phi_1(t)$, and $s_1(t) = s_{10}\phi_0(t)+s_{11}\phi_1(t)$. Here, $T_s = T_b$ since each symbol has only one bit.

Step 1 [Obtain $\psi_{0(t)}$ and hence $\phi_{0(t)}$]: For $i = 0$, using (A.4), we get,

$$\psi_0(t) = s_0(t). \tag{50}$$

So,

$$\phi_0(t) = \frac{s_0(t)}{\sqrt{\int_0^{T_b} s_0^2(t)dt}}. \tag{51}$$

Step 2 [Calculate s_{00} and s_{10}]:
Using (A.2), we write,

$$s_{00} = \int_0^{T_b} s_0(t)\phi_0(t)dt,$$
$$s_{10} = \int_0^{T_b} s_1(t)\phi_0(t)dt. \tag{52}$$

From (51) and (52), we get,

$$s_{00} = \sqrt{\int_0^{T_b} s_0^2(t)dt},$$
$$s_{10} = \frac{\int_0^{T_b} s_0(t)s_1(t)dt}{\sqrt{\int_0^{T_b} s_0^2(t)dt}} = \frac{\langle s_0(t), s_1(t)\rangle}{s_{00}}, \tag{53}$$

where $\langle . \rangle$ denotes the inner product operation.

Step 3 [Obtain $\psi_{1(t)}$ and hence $\phi_{1(t)}$]: For $i = 1$, we get from (A.4),

$$\psi_1(t) = s_1(t) - s_{10}\phi_0(t). \tag{54}$$

So,

$$\phi_1(t) = \frac{s_1(t) - s_{10}\phi_1(t)}{\sqrt{\int_{-\infty}^{+\infty} \psi_1^2(t)dt}}, \tag{55}$$

where

$$\int_{-\infty}^{+\infty} \psi_1^2(t)dt = \int_0^{T_b} s_1^2(t)dt - s_{10}^2. \tag{56}$$

Step 4 [Calculate s_{01} and s_{11}]: From (A.2), we get,

$$s_{01} = \int_0^{T_b} s_0(t)\phi_1(t)dt,$$
$$s_{11} = \int_0^{T_b} s_1(t)\phi_1(t)dt. \tag{57}$$

Using (A.7), the Euclidean distance between the two signals can be calculated as,

$$d = \sqrt{(s_{00} - s_{10})^2 + (s_{01} - s_{11})^2}. \tag{58}$$

For the binary case, the two received symbols are expressed, using (45), as

$$y_0(t) = s_0(t) + n(t),$$
$$y_1(t) = s_1(t) + n(t), \tag{59}$$

where $s_0(t) = \Re x_0(t)$, $s_1(t) = \Re x_1(t)$, and $n(t)$ is Gaussian noise with zero mean and a one-sided PSD of $\mathcal{N}_0$ given in (49). For maximum-likelihood (ML) detection, the total probability of error is [68],

$$P_e = \mathbb{Q}\left(\frac{d}{\sqrt{2\mathcal{N}_0}}\right). \tag{60}$$

Using the above method, we now calculate the error probability for VOOK and VPPM.

1) BER FOR VOOK

The orthogonal representation for VOOK is,

$$k_0(t) = k_{00}u_0(t) + k_{01}u_1(t),$$
$$k_1(t) = k_{10}u_0(t) + k_{11}u_1(t), \tag{61}$$

where k_{00}, k_{01}, k_{10} and k_{11} are constants independent of time, and $u_0(t)$ and $u_1(t)$ are two orthonormal functions. As described in Section II-A, the shapes of the VOOK signals are different for $\gamma \leq 0.5$ and $\gamma > 0.5$, so we have two cases.

Case-I [$\gamma \leq 0.5$]: We proceed using the signals for $\gamma \leq 0.5$ given in (1) and (2) and depicted in Fig. 2. Using (51), we get, $u_0(t) = 0$, which is obvious because one of the signals, $k_o(t)$, is zero and so we require only one orthogonal dimension. Consequently, from (52), we get, $k_{00} = k_{10} = 0$. Now, using (55) and (56), we can write,

$$u_1(t) = \frac{k_1(t)}{A\sqrt{2\gamma T_b}}, \tag{62}$$

which is illustrated in Fig. 15(a). Finally, from (57), we have $k_{01} = 0$ and $k_{10} = A\sqrt{2\gamma T_b}$. Hence, the Euclidean distance, in this case, is calculated to be $d_{\mathrm{K}} = A\sqrt{2\gamma T_b}$.

Case-II: [$\gamma > 0.5$]: We now orthogonalize the signals for $\gamma > 0.5$ shown in Fig. 2 and using (51), we have

$$u_0(t) = \frac{k_0(t)}{A\sqrt{(2\gamma - 1)T_b}}, \tag{63}$$

which can be substituted in (52), to get $k_{00} = k_{10} = A\sqrt{(2\gamma - 1)T_b}$. Similarly, using (55), we obtain the other basis function as,

$$u_1(t) = \frac{k_1(t)}{A\sqrt{2(1-\gamma)T_b}} - \sqrt{\frac{2\gamma - 1}{2(1-\gamma)}}u_0(t). \tag{64}$$

The two basis functions for VOOK when $\gamma > 0.5$ are depicted in Fig. 15(b). In Figs. 2 and 15(b), we observe that $k_0(t)$ and $u_1(t)$ do not overlap and so using (57), we get $k_{01} = 0$ and $k_{11} = A\sqrt{2(1-\gamma)T_b}$. Now, from (58), we determine the Euclidean distance to be $d_{\mathrm{K}} = A\sqrt{2(1-\gamma)T_b}$. To summarize, we have,

$$d_{\mathrm{K}} = \begin{cases} A\sqrt{2\gamma T_b}, & \gamma \leq 0.5 \\ A\sqrt{2(1-\gamma)T_b}, & \gamma > 0.5, \end{cases} \tag{65}$$

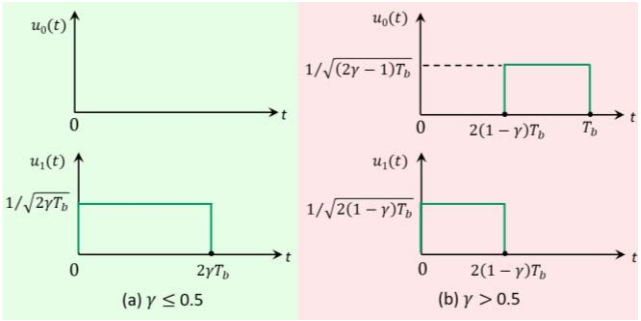

FIGURE 15. Orthonormal waveforms for VOOK when (a)$\gamma \leq 0.5$, and (b) $\gamma > 0.5$.

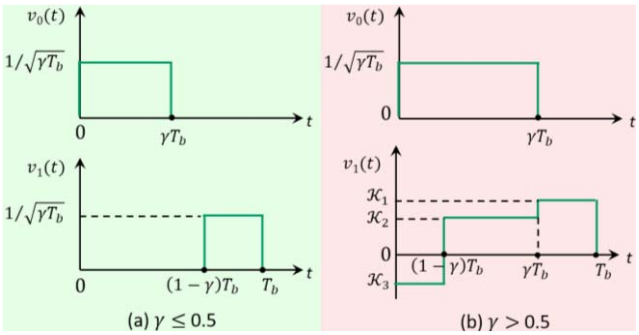

FIGURE 16. Orthonormal waveforms for VPPM when (a) $\gamma \leq 0.5$, and (b) $\gamma > 0.5$.

and finally, using (60) and (65), we get the BER for VOOK as

$$P_{e,\mathrm{K}} = \begin{cases} \mathbb{Q}\left(\sqrt{\gamma \frac{E_b}{\mathcal{N}_0}}\right), & \gamma \leq 0.5 \\ \mathbb{Q}\left(\sqrt{(1-\gamma)\frac{E_b}{\mathcal{N}_0}}\right), & \gamma > 0.5, \end{cases} \tag{66}$$

where $E_b = A^2 T_b$ is the energy per bit in the signals. The term $E_b/\mathcal{N}_0$ is also known as the normalized SNR.

2) BER FOR VPPM

We now orthogonalize the VPPM signals in (5) and (6), which can be written as,

$$\begin{aligned} p_0(t) &= p_{00} v_0(t) + p_{01} v_1(t), \\ p_1(t) &= p_{10} v_0(t) + p_{11} v_1(t), \end{aligned} \tag{67}$$

where p_{00}, p_{01}, p_{10} and p_{11} are constants independent of time, and $v_0(t)$ and $v_1(t)$ are the two orthonormal basis functions. Using (6) and (51), we get the first basis function as,

$$v_0(t) = \frac{p_0(t)}{A\sqrt{\gamma T_b}}, \tag{68}$$

which is illustrated in Figs. 16(a) and 16(b) for $\gamma \leq 0.5$ and $\gamma > 0.5$, respectively. Substituting this in (52), we get $p_{00} = A\sqrt{\gamma T_b}$. However, we observe that the calculations of p_{01} and other parameters depend on the overlap between $p_1(t)$ and $v_0(t)$ which, in turn, depends upon the value of γ. From Figs. 4 and 16, the limiting case of overlap is $(1-\gamma)T_b = \gamma T_b$, i.e., $\gamma = 0.5$. So we have two cases: $\gamma \leq 0.5$ and $\gamma > 0.5$.

Case-I: [$\gamma \leq 0.5$]: Here $(1-\gamma)T_b \geq \gamma T_b$ and so $p_1(t)$ and $v_0(t)$ do not overlap. Hence, using (52) we get, $p_{10} = 0$. The second basis function is obtained from (55) as,

$$v_1(t) = \frac{p_1(t)}{A\sqrt{\gamma T_b}}, \tag{69}$$

which can be graphically represented as shown in Fig. 16(a). Again, since $(1-\gamma)T_b \geq \gamma T_b$, so $p_0(t)$ and $v_1(t)$ do not overlap. Hence, using (57) we get, $p_{01} = 0$ but $p_1(t)$ and $v_1(t)$ overlap in the region $(1-\gamma)T_b \leq t \leq T_b$, and so, $p_{11} = A\sqrt{\gamma T_b}$. Finally, using (58), we calculate the Euclidean distance between the signals to be,

$$d_{\mathrm{P}} = A\sqrt{2\gamma T_b}. \tag{70}$$

Case-II: [$\gamma > 0.5$]: Here $(1-\gamma)T_b < \gamma T_b$ and so $p_1(t)$ and $v_0(t)$ overlap in the region $(1-\gamma)T_b \leq t \leq \gamma T_b$. From (52) we get, $p_{10} = A(2\gamma - 1)\sqrt{T_b/\gamma}$. Now, using (54 – 56), we obtain the second basis function as,

$$v_1(t) = \begin{cases} \sqrt{\frac{(1-2\gamma)^2}{\gamma(4\gamma-1-3\gamma^2)T_b}}, & 0 \leq t < (1-\gamma)T_b \\ \sqrt{\frac{(1-\gamma)^2}{\gamma(4\gamma-1-3\gamma^2)T_b}}, & (1-\gamma)T_b \leq t \leq \gamma T_b \\ \sqrt{\frac{\gamma}{(4\gamma-1-3\gamma^2)T_b}}, & \gamma T_b < t \leq T_b, \end{cases} \tag{71}$$

which is illustrated in Fig. 16(b) with $\mathcal{K}_3$, $\mathcal{K}_2$ and $\mathcal{K}_1$ being the signal levels in the three time-intervals, respectively, in (71). Note that, if the orthonormal function (being used to represent a signal) is negative, it does not necessarily imply that the signal itself is negative. Therefore, although, as depicted in Fig. 16(b), $v_1(t)$ for $\gamma > 0.5$ is negative during $0 \leq t < (1-\gamma)T_b$, the VPPM signal is always positive for all values of γ (ref. Fig. 4).

Substituting (71) in (57) yields $p_{01} = 0$ and $p_{11} = A\sqrt{(4\gamma - 1 - 3\gamma^2)T_b/\gamma}$. Hence, using (58), the Euclidean distance, in this case, is calculated to be $d_{\mathrm{P}} = A\sqrt{2(1-\gamma)T_b}$. We now summarize the results for VPPM as,

$$d_{\mathrm{P}} = \begin{cases} A\sqrt{2\gamma T_b}, & \gamma \leq 0.5 \\ A\sqrt{2(1-\gamma)T_b}, & \gamma > 0.5, \end{cases} \tag{72}$$

which is substituted in (60), to obtain the BER expression for VPPM given below:

$$P_{e,\mathrm{P}} = \begin{cases} \mathbb{Q}\left(\sqrt{\gamma \frac{E_b}{\mathcal{N}_0}}\right), & \gamma \leq 0.5 \\ \mathbb{Q}\left(\sqrt{(1-\gamma)\frac{E_b}{\mathcal{N}_0}}\right), & \gamma > 0.5. \end{cases} \tag{73}$$

Interestingly, the error performance of both the schemes is symmetric about $\gamma = 0.5$. Moreover, the Euclidean distance and hence, the BER expressions for VOOK and VPPM are the same. This observation has also been noted for NRZ-OOK and 2-PPM by authors in [69], [70].

VI. PERFORMANCE ANALYSIS

In this section, we study the effect of various system parameters (namely, dimming level, modulation scheme, data rate and channel equalization) on the BER performance of the system.

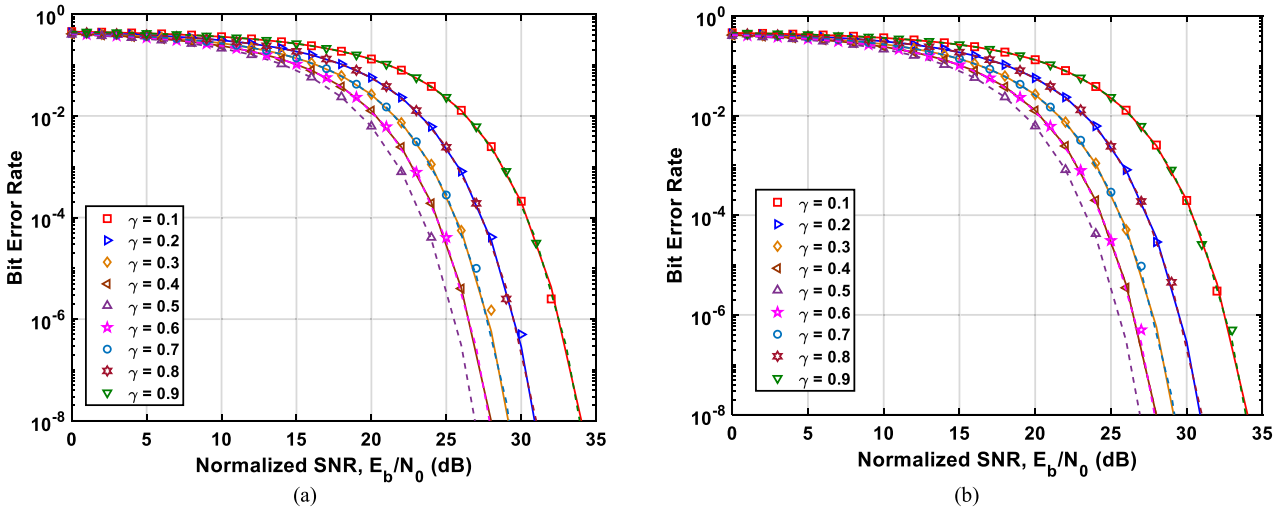

FIGURE 17. Variation of BER with increase in normalized SNR for (a) VOOK, and (b) VPPM with ZFE at different dimming levels (γ). Here, the markers indicate simulation results, and the dotted lines are analytical plots.

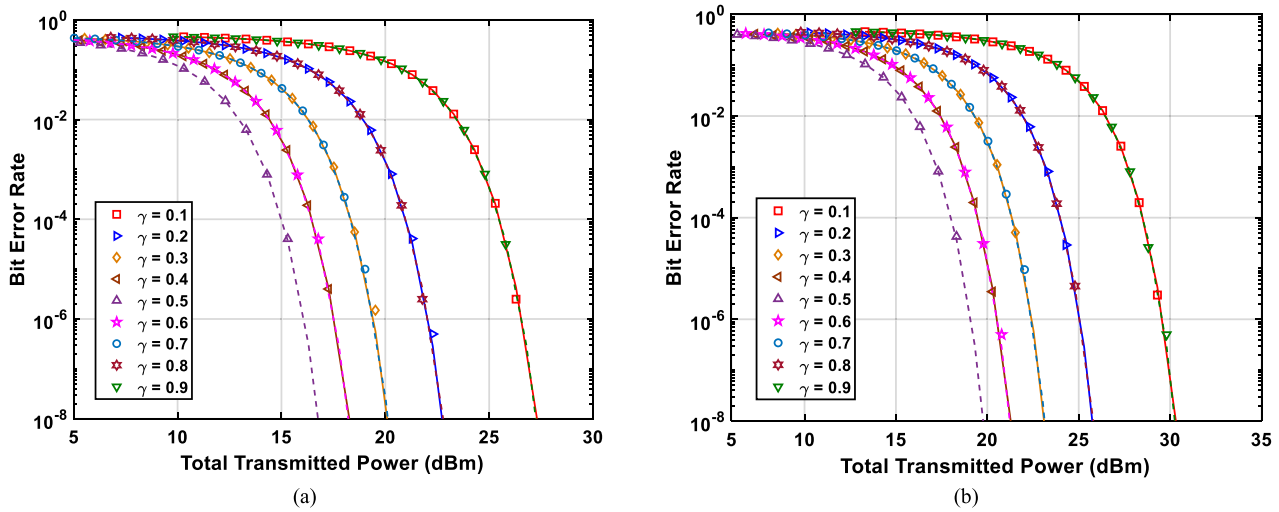

FIGURE 18. Variation of BER with increase in total transmitted power for (a) VOOK, and (b) VPPM with ZFE at different dimming levels (γ). Here, the markers indicate simulation results, and the dotted lines are analytical plots.

A. EFFECT OF DIMMING LEVEL

In Fig. 17(a), we plot the variation in BER for VOOK with an increase in normalized SNR (also denoted as $E_b/\mathcal{N}_0$) for different values of dimming levels where we observe that the BER curves at $\gamma = 0.1$, $\gamma = 0.2$, $\gamma = 0.3$ and $\gamma = 0.4$ are the same as those at $\gamma = 0.9$, $\gamma = 0.8$, $\gamma = 0.7$ and $\gamma = 0.6$, respectively, i.e., the BERs for γ and $1 - \gamma$ are equal. Hence, the error performance is symmetric about $\gamma = 0.5$. Moreover, as the dimming is increased above or decreased below $\gamma = 0.5$, the error performance deteriorates. Specifically, ~ 7 dB more SNR is required to maintain a BER of 10^{-6}, when γ is increased from 0.5 to 0.9 or reduced from 0.5 to 0.1. Furthermore, as depicted in Fig. 17(b), the BER vs. $E_b/\mathcal{N}_0$ curves for VPPM are the same as those for VOOK. Since these curves are plotted with respect to the normalized SNR, the effect of BW requirement is not considered herein, and hence, the BER curves for VOOK and VPPM are identical. All these observations are consistent with the results and explanations presented in Section V. Moreover, the simulation results (denoted by marker points) are in excellent agreement with the analytical results (represented by dotted curves).

For a more holistic evaluation, we include the effect of BW requirement and so, in all further analyses, we study the error performance with respect to the total transmitted power. For quantitative comparison, we define *power penalty* as the difference in power levels required to maintain a BER of 10^{-6} under two different system conditions. In Figs. 18(a) and 18(b), we depict the error performance of VOOK and VPPM, respectively, with respect to the total transmitted power at different dimming levels. In both cases, increasing γ from 0.5 to 0.9 (or reducing it from 0.5 to 0.1) incurs a power penalty of ~ 10 dB. Although the BER follows the same pattern with dimming as in Fig. 17, the BER curves of

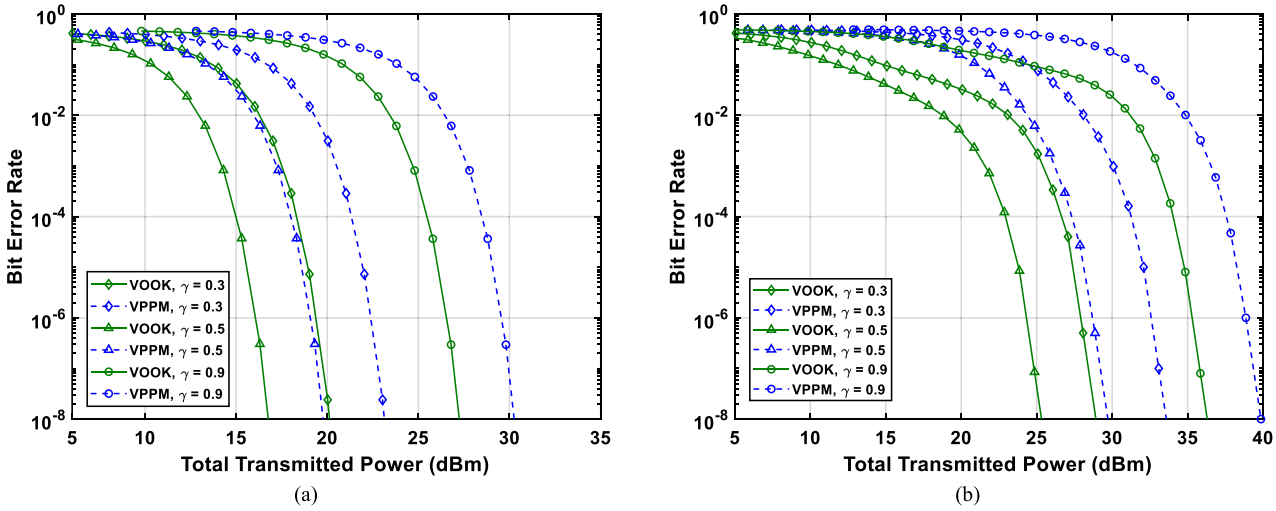

FIGURE 19. Variation of BER with increase in total transmitted power for VOOK and VPPM (a) with ZFE, and (b) without ZFE at different dimming levels (γ). Due to symmetricity around $\gamma = 0.5$, the BER plots for $\gamma = 0.1$ and $\gamma = 0.7$ (not shown here) are same as $\gamma = 0.9$ and $\gamma = 0.3$, respectively.

VOOK and VPPM are evidently different when plotted with respect to increase in transmitted power instead of $E_b/\mathcal{N}_0$. VPPM results in higher BER than VOOK. This is studied in greater detail in the following sub-section.

B. EFFECT OF MODULATION SCHEME

We now compare the error performance of the two dimming-based modulation schemes, namely, VOOK and VPPM. In Fig. 19(a), we depict the error performance of VOOK and VPPM with ZFE at different dimming levels. Since the BW requirement of VPPM is double that of VOOK, so its BER performance is poorer than VOOK. At all dimming levels, using VPPM instead of VOOK results in a power penalty of ~ 3 dB. A similar analysis is presented in Fig. 19(b) but without using the ZFE filter. The power penalty for using VPPM now increases to $\sim$ 5 dB. Moreover, the BER obtained without using ZFE is significantly higher than that obtained with ZFE. The performance enhancement achieved by using ZFE is analyzed in the next sub-section.

C. EFFECT OF CHANNEL EQUALIZATION

In this sub-section, we analyze the improvement in error performance due to ISI mitigation by the implementation of ZFE at $R_b = 660$ Mb/s. In Fig. 20(a), we study the BER performance of VOOK with and without ZFE at different dimming levels. We observe that without channel equalization, there is a power penalty of ~ 9 dB due to the presence of ISI. Similarly, for VPPM, as shown in Fig. 20(b), the power penalty is $\sim$ 10 dB if ZFE is not used. However, as explained in the next sub-section, the use of ZFE is not advantageous at low data rates.

D. EFFECT OF DATA RATE

When the data rate is high, the symbol duration is small and so, the delay spread is not negligible in comparison to the symbol period. Consequently, the effect of delay spread (and hence, ISI) becomes prominent [55], [61]. We now study the error performance at different data rates with and without channel equalization. For brevity, we fix the modulation scheme as VOOK and the dimming level at $\gamma = 0.5$. The effect of changing these parameters is explained in the previous sub-sections. In Fig. 21(a), we depict the error performance of VOOK at different data rates when ZFE is used. We infer that a power penalty of $\sim$ 18 dB is incurred when the data rate is increased from 50 Mb/s to 3 Gb/s. However, if ZFE is not used, as shown in Fig. 21(b), this power penalty increases to $\sim$ 30 dB due to the presence of ISI.

The effect of using channel equalization is depicted in Fig. 22 for some data rates. In Figs. 20–22, we observe that using ZFE is not advantageous at low data rates ($\leq$ 100 Mb/s). As explained in Section V-A, the implementation of ZFE mitigates ISI, but it also enhances the noise that is added by the receiver. At low data rates, where the effect of ISI is minimal, the benefit obtained by ISI mitigation due to ZFE is overshadowed by the noise enhancement at the receiver. Specifically, power penalties of $\sim$ 2.7 dB, $\sim$ 2.3 dB, and $\sim$ 1.4 dB are observed at data rates of 50 Mb/s, 75 Mb/s and 100 Mb/s, respectively. Hence, effectively, the use of ZFE results in the deterioration of BER performance at low data rates. However, at high data rates, the advantage of ISI mitigation surpasses the noise enhancement, resulting in a net improvement in error performance of the system. For example, from Figs. 20 – 22, we infer that using ZFE leads to a power saving of $\sim$1.5 dB at 250 Mb/s, increasing to $\sim$8.5 dB at 500 Mb/s and beyond. The power savings obtained at different data rates are listed in Table 2. In Fig. 23, the BER performance is studied for three different power levels at data rates 500 Mb/s to 3 Gb/s. Here again, we observe that channel equalization leads to significant improvements in the error performance of the system.

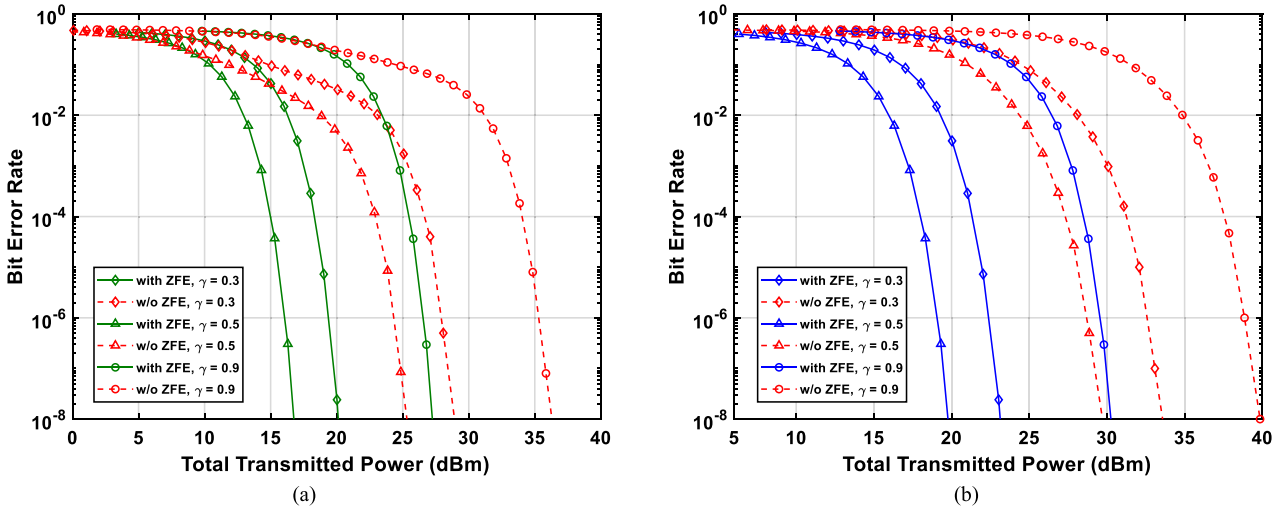

FIGURE 20. Variation of BER with increase in total transmitted power for (a) VOOK, and (b) VPPM with and without ZFE at different dimming levels (γ) when R_b = 660 Mb/s. Due to symmetricity around $\gamma = 0.5$, the BER plots for $\gamma = 0.1$ and $\gamma = 0.7$ (not shown here) are same as $\gamma = 0.9$ and $\gamma = 0.3$, respectively.

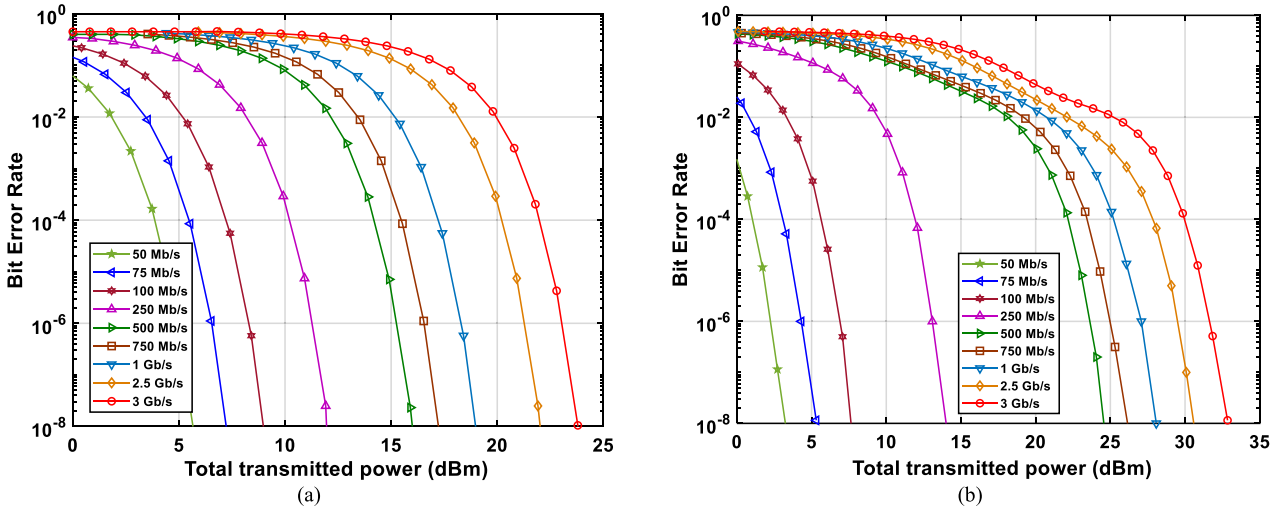

FIGURE 21. Variation of BER with increase in total transmitted power for VOOK (a) with ZFE, and (b) without ZFE at different data rates when $\gamma = 0.5$.

TABLE 2. Power savings for BER = 10^{-6}.

Data Rate R_b (Mb/s)	Power Required for BER = 10^{-6}		Power Saving (dB)
	Without ZFE (dBm)	With ZFE (dBm)	
50	2.44	5.18	−2.74
75	4.31	6.59	−2.28
100	6.96	8.34	−1.38
250	13.07	11.56	1.51
500	23.78	15.54	8.24
750	25.07	16.58	8.49
1000	27.08	18.33	8.75
2500	29.70	21.56	8.14
3000	31.67	23.31	8.36

Physical parameters (like LED semi-angle, detector FoV, detector size, etc.) also affect the BER performance of VLC systems. The impact of these factors manifests in a reduction of the SNR at the receiver. This has been extensively studied in the literature for conventional VLC systems (without dimming functionality) [6], [55], [58]. Detector area is directly related to the channel gain and so increasing the detector area enhances the gain leading to performance improvement. However, a very large detector area deteriorates performance due to the capture of spurious signals like ambient light, sunlight etc. [6]. Moreover, a detailed comprehensive study on the effect of LED semi- angle on the achievable data rate and BER of a multipath VLC system has been recently presented in [55], where it has been shown that with an increase in the LED semi-angle, the system performance first improves and then deteriorates, thereby indicating the existence of an optimum value of semi-angle at which the system performance is the best. Furthermore, in [58], the authors study the effect of detector FoV on the achievable data rate and received SNR of the system. They show that increasing the FoV degrades the system performance. However, a conventional

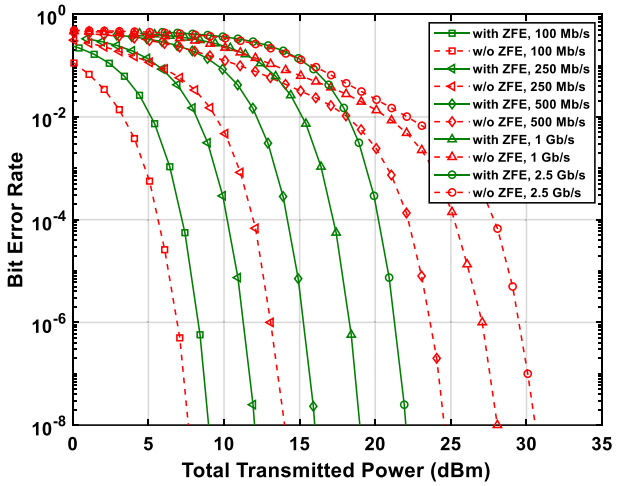

FIGURE 22. Variation of BER with increase in total transmitted power for VOOK with and without ZFE at different data rates when $\gamma = 0.5$.

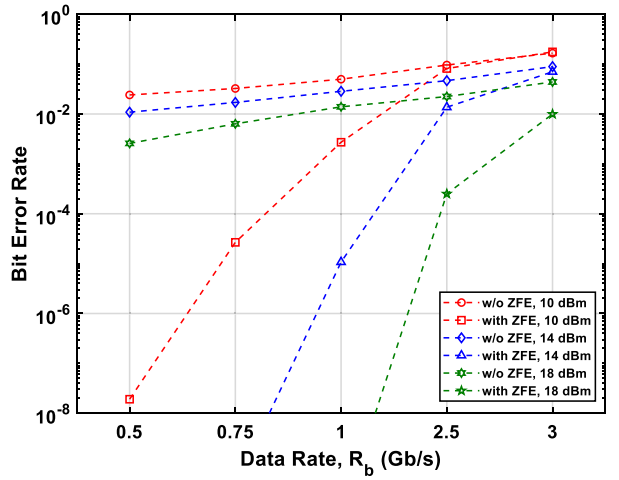

FIGURE 23. Variation of BER with increase in data rate for VOOK with and without ZFE at different values of total transmitted power when $\gamma = 0.5$.

VLC system designed to operate at acceptable values of target BER (generally chosen between $10^{-6} - 10^{-3}$) may not work reliably when the dimming functionality is incorporated therein. This is because, for dimmable VLC systems, the BER performance is aggravated if the reduction in transmitted power (at low levels of dimming) deteriorates the SNR such that the BER increases above the target value leading to unreliable system performance. Hence, while designing dimmable VLC systems, the physical parameters should be chosen such that the system performance is reliable (i.e., the BER remains below the target value chosen between $10^{-6} - 10^{-3}$) at all dimming levels, especially at low dimming values.

VII. CONCLUSION

In this paper, we propose the use of channel equalization to mitigate the effect of ISI and thereby improve the error performance of a dimmable VLC system. We obtain the analytical expression for the BER of dimming-based modulation schemes (namely, VOOK and VPPM) used in VLC and also study their spectral performance. We derive the expressions for PSDs of VOOK and VPPM and show that their spectra are significantly affected by the level of dimming. For both the schemes, the continuous part of the spectra are symmetrical around $\gamma = 0.5$, i.e., they are identical for γ and $1 - \gamma$. The discrete spectra for VOOK and VPPM are same, and both have high DC power and negligible non-DC spectral lines at high values of γ, leading to problems during AC coupling and clock recovery. We compare the different methods used to quantify the BW requirement and conclude that the "approximate BW" is the most reliable definition to evaluate the actual BW required by the dimming-based modulation schemes. Comparatively, VPPM requires double the BW required by VOOK, and hence, its spectral efficiency is half that of VOOK. Furthermore, we formulate the analytical model for the implementation of a ZFE filter to mitigate the effect of ISI on the system. We derive the BER of both schemes with ZFE and observe that the error performance is also identical for γ and $1-\gamma$. Moreover, the BER obtained with VPPM is more than that with VOOK. We also show that ZFE causes deterioration in the error performance at low data rates ($\leq$ 100 Mb/s), where the noise enhancement dominates the benefit of ISI mitigation. However, channel equalization is significantly advantageous at higher data rates where ISI is largely prevalent, and its mitigation leads to considerable improvement in system performance. The spectral analysis and ISI mitigation technique presented in this paper provide critical insights into the development of practical high data rate dimmable VLC systems. The work presented in this paper can be extended by studying other dimming-based modulation schemes and channel equalization techniques. Moreover, the effect of physical parameters (like LED semi-angle, detector FoV, detector size, etc.) on the performance of dimmable VLC systems can also be studied.

APPENDIX
GRAM-SCHMIDT ORTHOGONALIZATION PROCEDURE

In this Appendix, we describe the Gram-Schmidt orthogonalization procedure [68]. Developed by J. P. Gram in 1883, and later popularized by Erhard Schmidt in 1907, the procedure is commonly used in the signal-state analysis to represent any set of M energy signals as a linear combination of N orthonormal basis functions, such that $N \leq M$. So, for a set of real-valued energy signals, $s_0(t), s_1(t), \ldots, s_{M-1}(t)$, each of duration T_s, we can find a set of real-valued basis functions $\phi_0(t), \phi_1(t), \ldots, \phi_{N-1}(t)$, such that,

$$s_i(t) = \sum_{j=0}^{N-1} s_{ij}\phi_j(t), \tag{A.1}$$

where $i, j \in \mathbb{N}^+$, $0 \leq i \leq M-1$, $i \leq j \leq N-1$, and $\mathbb{N}^+$ is the set of non-negative integers. Hence, each signal in the set $\{s_i(t)\}$ is completely determined by the coefficients s_{ij} and the vector $\mathrm{s_i} = [s_{i0}\ s_{i1} \cdots s_{iN-1}]^{\mathrm{T}}$ is called the signal

vector corresponding to $s_i(t)$, where $[.]^{\mathrm{T}}$ denotes the matrix transpose operation. The coefficients s_{ij} are the projections of the signal $s_i(t)$ on the basis function $\phi_j(t)$, and are calculated by taking the inner product of $s_i(t)$ and $\phi_j(t)$ as,

$$s_{ij} = \int_0^{T_s} s_i(t)\phi_j(t)\ dt. \tag{A.2}$$

The basis functions are orthonormal, i.e., they must satisfy the following two conditions,

$$\int_0^{T_s} \phi_i(t)\phi_j(t)\ dt = \begin{cases} 0, & \text{if } i \neq j \\ 1, & \text{if } i = j. \end{cases} \tag{A.3}$$

While the first condition states that these functions are orthogonal to each other in the time period $0 \leq t \leq T_s$, the second condition specifies that they are normalized to have unit energy. Note that for a given signal set, the basis functions are not unique. They depend upon the sequence in which the orthogonalization is done, i.e., the signal that is designated as $s_1(t)$ and so on.

The first step in the orthogonal procedure is to define an intermediate function $\psi_i(t)$ which is obtained by subtracting from the i^{th} signal $s_i(t)$, the projections of $s_i(t)$ over all previous basis functions, i.e., $\phi_0(t), \phi_1(t), \ldots, \phi_{i-1}(t)$, i.e.,

$$\psi_i(t) = s_i(t) - \sum_{j=0}^{i-1} s_{ij}\phi_j(t), \tag{A.4}$$

where the coefficients s_{ij} are calculated using (A.2). From $\psi_i(t)$, we obtain the i^{th} basis function by dividing $\psi_i(t)$ by its length as,

$$\phi_i(t) = \frac{\psi_i(t)}{\sqrt{\int_{-\infty}^{+\infty} \psi_i^2(t)dt}}, \tag{A.5}$$

where,

$$\int_{-\infty}^{+\infty} \psi_i^2(t)dt = \int_0^{T_s} s_i^2(t)dt - \sum_{j=0}^{i-1} s_{ij}^2. \tag{A.6}$$

Note that, if the signals in the set $\{s_i(t)\}$ are not linearly independent, then $N < M$ and the intermediate functions $\psi_i(t) = 0$ for $i > N - 1$. However, if the signals are linearly independent then $N = M$. Now the Euclidean distance between any two signals $s_i(t)$ and $s_k(t)$ of this set is calculated as $d_{ik} = \|\mathrm{s_i} - \mathrm{s_k}\|$, where $\|.\|$ denotes the norm operation. Hence,

$$d_{ik} = \sqrt{\sum_{j=1}^{N} \left(s_{ij} - s_{kj}\right)^2}. \tag{A.7}$$

REFERENCES

[1] "IMT traffic estimates for the years 2020 to 2030," Int. Telecommun. Union, Geneva, Switzerland, ITU-Recommendation M.2370-0, Jul. 2015.

[2] L. Chettri and R. Bera, "A comprehensive survey on Internet of Things (IoT) toward 5G wireless systems," *IEEE Internet Things J.*, vol. 7, no. 1, pp. 16–32, Jan. 2020.

[3] M. Z. Chowdhury, M. Shahjalal, S. Ahmed, and Y. M. Jang, "6G wireless communication systems: Applications, requirements, technologies, challenges, and research directions," *IEEE Open J. Commun. Soc.*, vol. 1, pp. 957–975, 2020.

[4] R. Raj, K. Saxena, and A. Dixit, "Passive optical identifiers for VLC-based indoor positioning systems: Design, hardware simulation and performance analysis," *IEEE Syst. J.*, early access, Jul. 27, 2020, doi: 10.1109/JSYST.2020.3002585.

[5] M. A. Arfaoui *et al.*, "Physical layer security for visible light communication systems: A survey," *IEEE Commun. Surveys Tuts.*, vol. 22, no. 3, pp. 1887–1908, 3rd Quart., 2020.

[6] P. Nabavi and M. Yuksel, "Comprehensive design and prototype of VLC receivers with large detection areas," *J. Lightw. Technol.*, vol. 38, no. 16, pp. 4187–4204, Aug. 15, 2020.

[7] L. E. M. Matheus, A. B. Vieira, L. F. M. Vieira, M. A. M. Vieira, and O. Gnawali, "Visible light communication: Concepts, applications and challenges," *IEEE Commun. Surveys Tuts.*, vol. 21, no. 4, pp. 3204–3237, 4th Quart., 2019.

[8] S. Rajagopal, R. D. Roberts, and S.-K. Lim, "IEEE 802.15.7 visible light communication: Modulation schemes and dimming support," *IEEE Commun. Mag.*, vol. 50, no. 3, pp. 72–82, Mar. 2012.

[9] *IEEE Standard for Local and Metropolitan Area Networks—Part 15.7: Short-Range Wireless Optical Communication Using Visible Light*, IEEE Standard 802.15.7-2011, Sep. 2011.

[10] M. Rea, *Illumination Engineering Society of North America (IESNA) Lighting Handbook*, Illuminating Eng. Soc., New York, NY, USA, Jul. 2000.

[11] S. S. Virk and P. M. Nathan, "Comparative performance analysis of zero forcing, minimum mean square error and decision feedback equalizer," in *Proc. IEEE Int. Conf. Green Comput. Commun. Conserv. Energy (ICGCE)*, Chennai, India, Dec. 2013, pp. 136–139.

[12] H. Park and J. R. Barry, "Modulation analysis for wireless infrared communications," in *Proc. IEEE Int. Conf. Commun. (ICC)*, vol. 2, Jun. 1995, pp. 1182–1186.

[13] H. Park and J. R. Barry, "Performance of multiple pulse position modulation on multipath channels," *IEE Optoelectron.*, vol. 143, no. 6, pp. 360–364, Dec. 1996.

[14] H. Sugiyama and K. Nosu, "MPPM: A method for improving the band-utilization efficiency in optical PPM," *J. Lightw. Technol.*, vol. 7, no. 3, pp. 465–472, Mar. 1989.

[15] H. Park, "Performance bound on multiple-pulse position modulation," *Opt. Rev.*, vol. 10, no. 3, pp. 131–132, May 2003.

[16] G. E. Atkin and K.-S. L. Fung, "Coded multipulse modulation in optical communication system," *IEEE Trans. Commun.*, vol. 42, no. 234, pp. 574–582, Feb.–Apr. 1994.

[17] C. N. Georghiades, "Some implications of TCM for optical direct-detection channels," *IEEE Trans. Commun.*, vol. 37, no. 5, pp. 481–487, May 1989.

[18] I. Bar-David and G. Kaplan, "Information rates of photon-limited overlapping pulse position modulation channels," *IEEE Trans. Inf. Theory*, vol. 30, no. 3, pp. 455–464, May 1984.

[19] C. N. Georghiades, "Modulation and coding for throughput-efficient optical systems," *IEEE Trans. Inf. Theory*, vol. 40, no. 5, pp. 1182–1186, Sep. 1994.

[20] K. Lee and H. Park, "Modulations for visible light communications with dimming control," *IEEE Photon. Technol. Lett.*, vol. 23, no. 16, pp. 1136–1138, Aug. 2011.

[21] M. Tahir and A. B. Siddique, "Optimal brightness-rate control using VR-MPPM and its spectral analysis for VLC system," *IEEE Commun. Lett.*, vol. 16, no. 7, pp. 1125–1128, Jul. 2012.

[22] B. Bai, Z. Xu, and Y. Fan, "Joint LED dimming and high capacity visible light communication by overlapping PPM," in *Proc. Annu. Wireless Opt. Commun. Conf. (WOCC)*, Shanghai, China, May 2010, pp. 1–5.

[23] Z. Yang, M. Jiang, L. Zhang, and H.-Z. Tan, "Enhanced multiple pulse position modulation aided reverse polarity optical OFDM system with extended dimming control," *IEEE Photon. J.*, vol. 10, no. 3, pp. 1–17, Jun. 2018.

[24] A. B. Siddique and M. Tahir, "Bandwidth efficient multi-level MPPM encoding decoding algorithms for joint brightness-rate control in VLC systems," in *Proc. IEEE Global Commun. Conf. (GLOBECOM)*, Dec. 2014, pp. 2143–2147.

[25] S. Kaur, W. Liu, and D. Castor, *VLC Dimming Proposal IEEE P802.15 Working Group for Wireless Personal Area Networks (WPANs)*, document IEEE 802.15-15-09-0641-00-0007, InterDigital, Wilmington, DE, USA, Sep. 2009.

[26] J. H. Yoo, B. W. Kim, and S. Y. Jung, "Modelling and analysis of M-ary variable pulse position modulation for visible light communications," *IET Optoelectron.*, vol. 9, no. 5, pp. 184–190, Oct. 2015.

[27] C. Min *et al.*, "A novel method for constructing VLC equalizer with active-passive hybrid network," *IEEE Photon. J.*, vol. 12, no. 2, pp. 1–10, Apr. 2020.

[28] H. Zhang, A. Yang, L. Feng, and P. Guo, "Gb/s real-time visible light communication system based on white LEDs using T-bridge cascaded pre-equalization circuit," *IEEE Photon. J.*, vol. 10, no. 2, pp. 1–7, Apr. 2018.

[29] X. Li, B. Hussain, L. Wang, J. Jiang, and C. P. Yue, "Design of a 2.2-mW 24-Mb/s CMOS VLC receiver SoC with ambient light rejection and post-equalization for Li-Fi applications," *J. Lightw. Technol.*, vol. 36, no. 12, pp. 2366–2375, Jun. 15, 2018.

[30] L. Wang, X. Wang, J. Kang, and C. P. Yue, "A 75-Mb/s RGB PAM-4 visible light communication transceiver system with pre- and post-equalization," *J. Lightw. Technol.*, vol. 39, no. 5, pp. 1381–1390, Mar. 1, 2021.

[31] Z. Ghassemlooy, W. Popoola, and S. Rajbhandari, *Optical Wireless Communications: System and Channel Modelling With MATLAB*. Boca Raton, FL, USA: CRC Press, 2018.

[32] M. K. Jha, N. Kumar, and Y. V. S. Lakshmi, "NOMA MIMO visible light communication with ZF-SIC and MMSE-SIC," in *Proc. PhD EDITS*, Bangalore, India, Nov. 2020, pp. 1–2.

[33] A. Anusree and R. K. Jeyachitra, "Performance analysis of a MIMO VLC (visible light communication) using different equalizers," in *Proc. Int. Conf. Wireless Commun. Signal Process. Netw. (WiSPNET)*, Chennai, India, Mar. 2016, pp. 43–46.

[34] H. Shen, Y. Deng, W. Xu, and C. Zhao, "Rate-maximized zero-forcing beamforming for VLC multiuser MISO downlinks," *IEEE Photon. J.*, vol. 8, no. 1, pp. 1–13, Feb. 2016.

[35] S. Rajbhandari *et al.*, "Neural network-based joint spatial and temporal equalization for MIMO-VLC system," *IEEE Photon. Technol. Lett.*, vol. 31, no. 11, pp. 821–824, Jun. 2019.

[36] Z. Feng, C. Guo, Y. Yang, Z. Ghassemlooy, and C. Feng, "MMSE based spatial dimming scheme for multiuser MISO VLC systems," in *Proc. IEEE Globecom Workshops (GC Wkshps)*, Singapore, Dec. 2017, pp. 1–6.

[37] H. Yang, C. Chen, W.-D. Zhong, and A. Alphones, "Joint precoder and equalizer design for multi-user multi-cell MIMO VLC systems," *IEEE Trans. Veh. Technol.*, vol. 67, no. 12, pp. 11354–11364, Dec. 2018.

[38] M. W. Eltokhey, M. A. Khalighi, A. S. Ghazy, and S. Hranilovic, "Hybrid NOMA and ZF pre-coding transmission for multi-cell VLC networks," *IEEE Open J. Commun. Soc.*, vol. 1, pp. 513–526, 2020.

[39] Y. S. Hussein, M. Y. Alias, and A. A. Abdulkafi, "On performance analysis of LS and MMSE for channel estimation in VLC systems," in *Proc. IEEE Int. Colloq. Signal Process. Appl. (CSPA)*, Melaka, Malaysia, Mar. 2016, pp. 204–209.

[40] X. Chen and M. Jiang, "Adaptive statistical Bayesian MMSE channel estimation for visible light communication," *IEEE Trans. Signal Process.*, vol. 65, no. 5, pp. 1287–1299, Mar. 2017.

[41] X. Li *et al.*, "Wireless visible light communications employing feed-forward pre-equalization and PAM-4 modulation," *J. Lightw. Technol.*, vol. 34, no. 8, pp. 2049–2055, Apr. 15, 2016.

[42] P. Miao, G. Chen, X. Wang, Y. Yao, and J. A. Chambers, "Adaptive nonlinear equalization combining sparse Bayesian learning and Kalman filtering for visible light communications," *J. Lightw. Technol.*, vol. 38, no. 24, pp. 6732–6745, Dec. 15, 2020.

[43] M. Wolf and L. Grobe, "Block transmission with frequency domain equalization in the presence of colored noise," in *Proc. Int. Conf. Transp. Opt. Netw.*, Stockholm, Sweden. Jun. 2011, pp. 1–4.

[44] M. Zhang and Z. Zhang, "Fractionally spaced equalization in visible light communication," in *Proc. IEEE Wireless Commun. Netw. Conf. (WCNC)*, Shanghai, China, Apr. 2013, pp. 4282–4287.

[45] H. Farahneh, F. Hussain, R. Hussain, and X. Fernando, "A novel optimal precoder and equalizer in 2×2 MIMO VLC systems for vehicular application," in *Proc. IEEE Globecom Workshops (GC Wkshps)*, Dec. 2018, pp. 1–6.

[46] Y. Li, I. Ngebani, X.-G. Xia, and A. Host-Madsen, "On performance of vector OFDM with linear receivers," *IEEE Trans. Signal Process.*, vol. 60, no. 10, pp. 5268–5280, Oct. 2012.

[47] C.-Y. Hsu and W.-R. Wu, "Low-complexity ICI mitigation methods for high-mobility SISO/MIMO-OFDM systems," *IEEE Trans. Veh. Technol.*, vol. 58, no. 6, pp. 2755–2768, Jul. 2009.

[48] C. Yoon, J. Son, and S. Lee, "A novel ZF detection scheme for double SFBC based OFDM system in frequency selective fading channel," in *Proc. IEEE Int. Conf. Commun. (ICC)*, Jun. 2007, pp. 2557–2561.

[49] J. Gancarz, H. Elgala, and T. D. C. Little, "Impact of lighting requirements on VLC system," *IEEE Commun. Mag.*, vol. 51, no. 12, pp. 34–41, Dec. 2013.

[50] M. Dyble, N. Narendran, A. Bierman, and T. Klein, "Impact of dimming white LEDs: Chromaticity shifts due to different dimming methods," in *Proc. SPIE*, vol. 5941, pp. 59411H1–59411H9, Sep. 2005.

[51] S. Beczkowski and S. Munk-Nielsen, "LED spectral and power characteristics under hybrid PWM/AM dimming strategy," in *Proc. IEEE Energy Convers. Congr. Expo.*, Sep. 2010, pp. 731–735.

[52] F. Zafar, D. Karunatilaka, and R. Parthiban, "Dimming schemes for visible light communication: The state of research," *IEEE Wireless Commun.*, vol. 22, no. 2, pp. 29–35, Apr. 2015.

[53] S. G. Wilson, *Digital Modulation and Coding*. Upper Saddle River, NJ, USA: Pearson Educ., 2003.

[54] F. Amoroso, "The bandwidth of digital data signal," *IEEE Commun. Mag.*, vol. 18, no. 6, pp. 13–24, Nov. 1980.

[55] R. Raj, S. Jaiswal, and A. Dixit, "On the effect of multipath reflections in indoor visible light communication links: Channel characterization and BER analysis," *IEEE Access*, vol. 8, pp. 190620–190636, 2020.

[56] R. Raj, S. Jaiswal, and A. Dixit, "Optimization of LED semi-angle in multipath indoor visible light communication links," in *Proc. IEEE Int. Conf. Adv. Netw. Telecommun. Syst. (ANTS)*, Goa, India, Dec. 2019, pp. 1–6.

[57] J. M. Kahn and J. R. Barry, "Wireless infrared communications," *Proc. IEEE*, vol. 85, no. 2, pp. 265–298, Feb. 1997.

[58] T. Komine and M. Nakagawa, "Fundamental analysis for visible-light communication system using LED lights," *IEEE Trans. Consum. Electron.*, vol. 50, no. 1, pp. 100–107, Feb. 2004.

[59] Z. Zhou, C. Chen, and M. Kavehrad, "Impact analyses of high-order light reflections on indoor optical wireless channel model and calibration," *J. Lightw. Technol.*, vol. 32, no. 10, pp. 2003–2011, May 15, 2014.

[60] E. Sarbazi, M. Uysal, M. Abdallah, and K. Qaraqe, "Ray tracing based channel modeling for visible light communications," in *Proc. 22nd Signal Process. Commun. Appl. Conf. (SIU)*, Trabzon, Turkey, Apr. 2014, pp. 702–705.

[61] J. R. Barry, J. M. Kahn, W. J. Krause, E. A. Lee, and D. G. Messerschmitt, "Simulation of multipath impulse response for indoor wireless optical channels," *IEEE J. Sel. Areas Commun.*, vol. 11, no. 3, pp. 367–379, Apr. 1993.

[62] Y. Wu, P. Audenaert, M. Pickavet, and D. Colle, "Mirror-aided non-LOS VLC channel characterizations with a time-efficient simulation model," *Photon. Netw. Commun.*, vol. 38, no. 1, pp. 151–166, Feb. 2019.

[63] J. Ding, Z. Xu, and L. Hanzo, "Accuracy of the point-source model of a multi-LED array in high-speed visible light communication channel characterization," *IEEE Photon. J.*, vol. 7, no. 4, pp. 1–14, Aug. 2015.

[64] J. Ding, K. Wang, and Z. Xu, "Impact of different LED-spacing in arrayed LED transmitter on VLC channel modeling," in *Proc. Int. Conf. Wireless Commun. Signal Process. (WCSP)*, Hefie, China, Oct. 2014, pp. 1–6.

[65] F. Miramirkhani and M. Uysal, "Channel modeling and characterization for visible light communications," *IEEE Photon. J.*, vol. 7, no. 6, pp. 1–16, Dec. 2015.

[66] M. Uysal *et al.*, *Optical Wireless Communications: An Emerging Technology*. Cham, Switzerland: Springer, Aug. 2016.

[67] S. Jaiswal, R. Raj, and A. Dixit, "Performance evaluation of multipath VLC links for different transmitter configurations," in *Proc. IEEE Int. Conf. Adv. Netw. Telecommun. Syst. (ANTS)*, Delhi, India, Dec. 2019, pp. 1–6.

[68] S. Haykin, *Digital Communication*. New York, NY, USA: Wiley, 1988.

[69] T. Y. Elganimi, "Studying the BER performance, power- and bandwidth- efficiency for FSO communication systems under various modulation schemes," in *Proc. IEEE Appl. Electr. Eng. Comput. Technol. (AEECT)*, Amman, Jordan, Dec. 2013, pp. 1–6.

[70] M. H. Ibrahim, H. A. Shaban, and M. H. Aly, "Effect of different weather conditions on BER performance of single-channel free space optical links," *Optik*, vol. 137, pp. 291–297, May 2017.